

***In situ* measurement of slow solar wind emerging from a pseudostreamer: a conjunction study with Parker Solar Probe and Solar Orbiter**

TAMAR ERVIN ^{1,2} STUART D. BALE ^{1,2} SAMUEL T. BADMAN ³ YEIMY J. RIVERA ³ ORLANDO ROMEO ^{4,2}
JIA HUANG ² PETE RILEY ⁵ TREVOR A. BOWEN ² SUSAN T. LEPRI ⁶ AND RYAN M. DEWEY ⁶

¹*Department of Physics, University of California, Berkeley, Berkeley, CA 94720-7300, USA; tamarervin@berkeley.edu*

²*Space Sciences Laboratory, University of California, Berkeley, CA 94720-7450, USA*

³*Center for Astrophysics | Harvard & Smithsonian, 60 Garden Street, Cambridge, MA 02138, USA*

⁴*Department of Earth and Planetary Science, University of California, Berkeley, CA 94720, USA*

⁵*Predictive Science Inc., San Diego, CA 92121, USA*

⁶*Department of Climate and Space Sciences and Engineering, University of Michigan, Ann Arbor, MI 48109, USA*

ABSTRACT

We seek to identify the source regions of the slow solar wind (SSW) through combining models with in situ observations. We leverage an opportune conjunction between Solar Orbiter and Parker Solar Probe (PSP) during PSP Encounter 11 to include compositional diagnostics from the Solar Orbiter heavy ion sensor (HIS) as these variations provide crucial insights into the origin and nature of the solar wind. We use Potential Field Source Surface (PFSS) and Magnetohydrodynamic (MHD) models to connect the observed plasma at PSP and Solar Orbiter to its origin footpoint in the photosphere, and compare these results with the in situ measurements. A very clear signature of a heliospheric current sheet (HCS) crossing as evidenced by enhancements in low FIP elements, ion charge state ratios, proton density, low-Alfvénicity, and polarity estimates validates the combination of modeling, data, and mapping. Fast wind from a small equatorial coronal hole (CH) with low ion charge state ratios, low FIP bias, high-Alfvénicity, and low footpoint brightness mostly fits together, yet includes anomalously low alpha particle abundance. We identify slow wind from many different sources, with broad variation in composition and Alfvénicity. We distinguish between classical non-Alfvénic and high-Alfvénicity SSW and make the association of low-Alfvénicity, decreased alpha-to-proton abundance, high charge state ratios, and FIP bias with streamer wind while intermediate alpha abundance, high-Alfvénicity, and dips in ion charge state ratios correspond to CH boundaries. Through this comprehensive analysis, we highlight the power of multi-instrument conjunction studies in assessing the sources of the solar wind.

1. INTRODUCTION

The solar wind is a stream of ionized plasma (composed of protons, electrons, and alphas along with trace amounts of heavy ions) that continuously escapes from the Sun and interacts with everything in its path (Parker 1958). While the parameters of the solar wind, such as density, velocity, and ion and elemental composition are highly variable, we can categorize the solar wind into distinct types. The main categorization is set using speed where slow and fast wind have a canonical cutoff between the two of 500 km s⁻¹ at 1AU (Zurbuchen 2007; Borovsky 2012; Stakhiv et al. 2015), however, there are other characteristics which can be used to differentiate types of solar wind: e.g. Alfvénicity (D’Amicis & Bruno 2015; Stansby et al. 2020b), particle densities (Mostafavi et al. 2022), and heavy ion composition (Widing & Feldman 2001; Zhao et al. 2009; Stansby et al. 2020a). While we have decades of measurements of solar wind parameters, we still lack a complete understanding of the acceleration, heating mechanisms, and source regions of the solar wind (Abbo et al. 2016; Cranmer & Winebarger 2019; Viall & Borovsky 2020). A better understanding of these mechanisms will come from making an effective connection between measurements taken in the heliosphere and relating them to their source region. Ideally, we aim to grasp the complete narrative spanning from the conditions of origination in the corona, through the subsequent evolution, to the moment when spacecraft intercept them in the heliosphere to create a more holistic picture of solar activity and the underlying mechanisms driving the solar wind.

It has been well established through studying Ulysses data covering a large range of heliographic latitudes that during solar minimum high-speed wind primarily originates from polar coronal holes (McComas et al. 1998, 2008). von Steiger et al. (2000) confirmed that faster wind had a more photosphere-like composition in comparison to slow wind, which supported the idea that elemental composition could be used to determine whether wind originated from a coronal hole (CH), active region, or streamer structures at the Sun. While fast solar wind is known to originate from CHs, the origins of the slow solar wind are not as well understood (Viall & Borovsky 2020). At solar minimum, slow wind has been observed primarily near the heliospheric current sheet (Bavassano et al. 1997; Smith et al. 1978), while during solar maximum it has been shown to be more interspersed with fast streams (McComas et al. 2001, 2008). The slow solar wind typically shows more variability (e.g. density, temperature, and chemical makeup) in comparison to the more homogeneous fast solar wind (FSW) (Bruno et al. 1986; Lopez & Freeman 1986; Schwenn 2006), exhibiting larger proton density, higher electron temperature, enhanced charge state ratios (C^{6+}/C^{5+} , O^{7+}/O^{6+}) and enhancement of elements of low first ionization potential (FIP) (von Steiger et al. 2000; Abbo et al. 2016, and references therein).

The large variability observed in the parameters of the slow wind suggests that it originates from a diverse set of source regions, likely influenced by position within the solar cycle, as different regions emerge at various stages. Studies using in situ measurements have found that some slow solar wind shows plasma signatures that are very similar to that of the FSW – high alpha particle abundances (Ohmi et al. 2004), large differential velocities (Stansby et al. 2020a), lower heavy ion charge state ratios and reduced low-FIP enhanced elemental abundances (Stakhiv et al. 2015; D’Amicis et al. 2018), and high Alfvénicity (D’Amicis & Bruno 2015; Perrone et al. 2020; D’Amicis et al. 2021). These are typical characteristics of the FSW, which means that it is likely that at least some of the slow solar wind originates from CHs, particularly small CHs or the boundaries of larger ones such that the coronal magnetic field strongly over expands. Wang & Sheeley (1990). D’Amicis & Bruno (2015); Stansby et al. (2018); Stansby et al. (2020b) and others have shown the existence of two types of slow solar wind: the classical slow solar wind (SSW) with slow speeds and low-Alfvénicity, and the highly Alfvénic slow solar wind (SASW) which shows properties more similar to that of the FSW.

There are a variety of theories using modeling and observational evidence that show the variance in possible sources of the slow solar wind. Eselevich et al. (1999); Riley & Luhmann (2012); Wang et al. (2012); Wang & Panasenco (2019); Panasenco & Velli (2013); Owens et al. (2014); Abbo et al. (2015) and others have shown slow solar wind originating from pseudostreamers – coronal streamers that separate open field lines of the same polarity (Wang et al. 2007). More recent work, such as by D’Amicis et al. (2021); Telloni et al. (2023); Velli et al. (2020); Panasenco et al. (2020), have used PSP and Solar Orbiter data to study the emergence of solar wind from pseudostreamers. Pseudostreamers consist of multipolar regions of magnetic field which open in a unipolar fashion to interplanetary space, thus separating two coronal holes of the same polarity (Wang et al. 2007). Chitta et al. (2023); Lynch et al. (2023) show that the S-web, a complex web of magnetic separatrices formed by small equatorial CHs reshaping the streamer belt, which reconnects in the middle corona, could drive the slow solar wind. Helmet streamer/streamer belt wind has been shown to contribute to some of the SSW high in the solar atmosphere ($5R_{\odot}$) (Sheeley et al. 1997), which is a different physical process than the steady outflow starting from the photosphere. Antiochos et al. (2011) showed that the heliospheric extension of the streamer belt, the heliospheric current sheet (HCS), is a source of SSW as well. This type of wind from the streamer belt and HCS is generally thought of as the classical SSW, having low Alfvénicity and typical SSW properties. Contrary to the SSW, SASW streams have been associated with origins at CH boundaries or small equatorial CHs (D’Amicis et al. 2021). Additionally, there is the possibility of active region contributions to the SSW during solar maximum (Kasper et al. 2016; Alterman et al. 2018; Alterman & Kasper 2019; Stansby et al. 2021).

A major difference in terms of the type of CH region expected to produce fast versus slow wind is the point at which the wind becomes supersonic (the critical point). Heating above this point causes increases in wind speed (Leer & Holzer 1980), and since rapidly diverging fields have higher critical points, they produce slower speed winds (Wang et al. 2012; Stansby et al. 2020b). Since small CHs have higher magnetic expansion, they are more likely to produce SSW due to the point of energy deposit in the magnetic structure (Nolte et al. 1976; Garton et al. 2018). This overall correspondence between magnetic expansion and solar wind speed as been well established empirically (Wang & Sheeley 1990) and forms the basis of the Wang-Sheeley-Argé solar wind prediction model (Argé & Pizzo 2000; Argé et al. 2003; Argé et al. 2004).

The solar wind is primarily comprised of ionized hydrogen (H) and helium (He), i.e. protons and alpha particles. Their properties, such as velocity, density, and temperature, vary and alpha particles are found at much lower number

densities when compared with protons (Bame et al. 1977). The enhancement or depletion in the alpha-to-proton abundance ratio is characteristic of FSW and HCS crossings, respectively. Suess et al. (2009) confirms the existence of alpha particle depletions up to 10 days in width and show that, alongside Borrini et al. (1981); Gosling et al. (1981), this depletion originates from helmet streamers in closed coronal loops due to transient plasma release from streamer cores which are then sheared due to velocity differences between the plasma from then two streamer legs (Suess et al. 2009). At solar minimum, the alpha abundance ratio shows significant positive correlation with wind speed, while at solar maximum the correlation is much weaker and converges to the fast wind ratio (4-5%), which is unchanged through the solar cycle (Kasper et al. 2007; Kasper et al. 2012). This is interpreted as showing that low alpha abundance slow solar wind comes from the HCS and helmet streamers, which are much more frequently sampled at solar minimum. Kasper et al. (2016); Alterman et al. (2018); Alterman & Kasper (2019) have shown that the combination of ‘alpha particle rich’ and ‘poor’ populations in the slow solar wind thus likely originate from solar minimum helmet streamers (alpha particle poor) and active regions (alpha particle rich).

In addition to hydrogen and helium, there are also small amounts of heavier ions ($Z > 2$) in the solar wind (Bame et al. 1977; Bochsler 2007). In the photosphere, hydrogen has an abundance of 12.00 while helium is at 10.914 ± 0.013 , oxygen (O) at 8.69 ± 0.04 , and iron (Fe) at 7.46 ± 0.04 (Asplund et al. 2021) where the abundance is $\log \epsilon_X = \log(N_X/N_H) + 12$. We use the photospheric elemental composition values for individual elements as context to understand how abundance values change elsewhere in the solar atmosphere (Asplund et al. 2009). The processes that ionize and fractionate the heavy ions lead to composition variations, which can be measured both via remote and in situ methods and occur either in the corona or chromosphere. Therefore, the composition of the solar wind is dependent upon the processes at work in the transition layers in the upper solar atmosphere (Laming et al. 2019). In this work, we look at the Fe/O ratio as a measure of fractionation (changes in elemental abundances summed over charge states) and FIP bias, and the ion charge state ratios of O^{7+}/O^{6+} and C^{6+}/C^{4+} as a measure of ionization level. The ion charge ratios are useful for studying the properties of the plasma from which the solar wind originates due to the ‘freeze in’ process whereby the ionization state remains constant beyond a certain distance from the solar surface, known as the freeze in point. This occurs because ionization and recombination rates are proportional to the electron density, which rapidly decreases with radial distance from the solar surface until the density is so low that neither of these processes can occur (Owocki et al. 1983). These ratios are then ‘frozen in’, at a freeze in point of 1.0 - $1.9R_\odot$ (Buergi & Geiss 1986; Chen et al. 2003; Landi et al. 2012), such that they can be used to determine information about the properties of the coronal plasma from which the wind originates.

C^{6+}/C^{4+} and O^{7+}/O^{6+} ratios are mainly set by the electron source temperature along with some (quite small) radial evolution effects upon reaching an open magnetic field line (Hundhausen 1968). Higher ion charge ratios are correlated with higher temperature source regions in the corona (Owens 2018). Thus, low O^{7+}/O^{6+} ratios imply solar wind originating from cold CH regions (von Steiger & Zurbuchen 2011, and references therein), however high O^{7+}/O^{6+} ratios have been shown to originate from multiple sources: active regions (Liewer et al. 2003; Ko et al. 2006, 2014; Culhane et al. 2014), CH boundaries (Antiochos et al. 2012; Crooker et al. 2012), and the helmet streamer stalk (Zhao et al. 2009, 2014; Zhao & Fisk 2011). Wang (2016) show that high O^{7+}/O^{6+} ratios are correlated with flux tubes emerging from the inner boundaries of CHs and that at 1AU, a threshold value of 0.145 separates CH wind of low O^{7+}/O^{6+} ratio from streamer wind (high O^{7+}/O^{6+} ratio). While this threshold was determined using measurements at 1AU, it can be applied to measurements closer to the Sun as the freeze-in of ionization states leads to minimal radial propagation effects on this ratio. Both the C^{6+}/C^{4+} and O^{7+}/O^{6+} ratios are expected to follow the same trends as they have similar freeze-in heights where the theoretically predicted temperature is monotonically increasing until its maximum, and thus, we expect the charge state ratios to be correlated. However, Zhao et al. (2017) discuss a type of ‘Outlier’ slow solar wind with C^{6+}/C^{5+} ratios much lower than expected that must originate at $1.6R_\odot$ or higher through an episodic generating process.

In addition to ion charge state ratios, studying FIP bias through the Fe/O ratio provides an additional tracer of coronal source region for comparison with model results. The FIP effect, in which the abundance of lower FIP elements (e.g. Fe) are observed to be enhanced relative to the abundance of higher FIP elements (e.g. O), was first measured in the solar wind and Solar Energetic Particles (SEPs), then later from spectroscopic coronal observations (Meyer 1985; Bochsler et al. 1986; Gloeckler & Geiss 1989; Feldman 1992). Remote measurements of coronal loops show that they exhibit FIP bias that increases the longer the loops exist (Feldman & Marsch 1997), and since some slow wind exhibits this type of bias, this indicates that this slow wind likely originates from large loops. In CH regions, we see continuously open field lines, while in other regions, material is trapped and released from large loops that sometimes

connect with open field lines. Therefore, coronal material escaping from structures such as streamers or active regions is distinct from material originating from CHs.

In the low chromosphere, the leading theory is that the majority of MHD waves that accelerate the solar wind are generated from convection-driven motions as pressure changes from thermal to magnetically dominated (Laming et al. 2019). In the upper chromosphere, neutral gas becomes ionized plasma leading to strong density gradients, which cause Alfvén wave refraction and reflection. This generates the ponderomotive force, which stems from the combination of reflection and refraction of Alfvén waves on plasma ions. Due to the electromagnetic nature of these waves, only ions feel this force. The time average of this force leads to an enhancement of ions over neutrals as it is directed upwards in the solar chromosphere (Laming 2017), which gives way to ion-neutral separation and the elemental fractionation (the FIP effect) in the upper atmosphere.

CHs undergo quasi-rigid rotation as the coronal field is continuously undergoing reconnection to remain close to a potential state (Lionello et al. 2005; Wang 2009). This continuous magnetic reconnection is thought to contribute to outwardly propagating MHD waves and heating that occurs far above the transition region. In the large loops that contribute to the slow solar wind, MHD waves remain trapped in the transition region, within regions of rapidly diverging open flux where heating is concentrated at low heights (Wang et al. 2009), thus heating the ions leading to enhanced charge state ratios. Additionally, the timescale for fractionation is typically 2 to 3 days, meaning plasma must remain in the corona for this time period to experience fractionation (Laming 2015). This is why plasma from open field lines that quickly escapes the corona does not see an enhancement in low-FIP abundances, while plasma on closed loops (e.g. those found in active regions forming the streamer belt) does (Geiss et al. 1995; von Steiger et al. 2000). We have discussed above a range of possible slow wind sources thus, we expect to see a wide range of FIP bias in the slow wind from different sources, and relatively low-FIP fractionation in the FSW originating from open magnetic field lines. We use the Fe/O measurement in conjunction with Alfvénicity, modeling efforts, and other in situ measurements to provide more powerful diagnostics of different types of solar wind and their source region.

In this study, we seek to characterize the source regions of both SASW and SSW through a combination of modeling methods and in situ diagnostics, leveraging a unique conjunction opportunity between inner heliospheric space missions. Understanding the origins of the slow wind will bring us closer to creating a comprehensive model for space weather predictions and allow us to better understand the impact of the solar wind on the near-Earth environment. We begin with a discussion of the spacecraft and remote sensing data that is used in this study in Section 2. We outline the advancements of Parker Solar Probe (PSP; Fox et al. (2016)) and Solar Orbiter (Müller, D. et al. (2020)) that allow for this study and how modeling methods are used in conjunction with in situ data to study the source regions of the solar wind. In Section 3, we discuss the two major magnetic field modeling methods used, potential field source surface (PFSS) and magnetohydrodynamic (MHD) models, and how these methods allow us to study the large-scale coronal magnetic field and identify solar wind source regions. We discuss the observations in Section 4 specifically looking at elemental composition (Section 4.1), particle velocity and abundance ratios (Section 4.2), and modeling efforts (Section 4.3). Lastly, in Section 5, we discuss the main results of the study, then finish with our conclusions and ideas for further work in Section 6.

2. DATA

Our study uses a combination of in situ data from PSP (Fox et al. 2016) and Solar Orbiter (Müller, D. et al. 2020) along with magnetograms from the Helioseismic and Magnetic Imager (HMI; Scherrer et al. (2012)) aboard the Solar Dynamics Observatory (SDO; Pesnell et al. (2012)) and the Global Oscillation Network Group (GONG; Harvey et al. (1996)) during the 11th solar encounter of PSP (E11) in February 18 to March 4, 2022. Through novel measurements, orbital trajectories and instrumentation methods, these instruments have revolutionized our study and understanding of the Sun. The combination of in situ measurements from PSP and Solar Orbiter coupled with modeling results using magnetograms from HMI/SDO and GONG allows us to characterize the solar wind and study its origins. The use of both PSP and Solar Orbiter data is required as Solar Orbiter provides elemental abundance measurements (such as the Fe/O ratio) and charge state ratios (C^{6+}/C^{4+} and O^{7+}/O^{6+}), which PSP does not, and PSP provides a much better quality calculation of Alfvénicity (see Appendix 8). Additionally, as PSP measures solar wind velocities all below the canonical 500 km s^{-1} cutoff during this time period, Solar Orbiter velocity measurements (which are closer to the asymptotic 1AU values) are necessary to characterize the wind as fast or slow according to the canonical 1AU cutoff. Lastly, measuring and identifying features at two substantially different heliocentric distances adds robustness to the analysis by verifying the relevant streams are long-lived and not strongly affected by transients or time evolution.

The PSP mission consists of four instruments to study coronal heating, particle acceleration, and energy flow through the corona: the Electromagnetic Fields Investigation (FIELDS; Bale et al. (2016)), the ‘Solar Wind Electrons, Alphas, and Protons’ (SWEAP; Kasper et al. (2016)) investigation, the Integrated Science Investigation of the Sun (IS \odot IS; McComas et al. (2016)), and the Wide-field Imager for Solar Probe (WISPR; Vourlidas et al. (2016)). From PSP/FIELDS, we use DC magnetic field measurements from the fluxgate magnetometer in radial-tangential-normal (RTN) coordinates (Bale et al. 2016). Proton and alpha particle measurements (density and velocity) from PSP come from the Ion Solar Probe ANalyzer (SPAN-I; Livi et al. (2022)) on PSP/SWEAP. The core electron density was estimated by fitting a bi-Maxwellian distribution along all pitch angles using SPAN-E 3D electron velocity distribution functions (VDFs) (Whittlesey et al. 2020), following a similar method by Romeo et al. (2023). Typically, electron density measurements are calculated from the quasithermal noise spectrum of measurements taken by the Radio Frequency Spectrometer on PSP (Pulupa et al. 2017), however, the instrument was not functioning for a large portion of E11, and thus this measurement is unusable for this time period. The proton and alpha data are cleaned based on the field of view (FOV) of the instrument and through comparison with electron density measurements. All E11 data used in this study is publicly available for download from the PSP/FIELDS ¹ and PSP/SWEAP data archives ².

The Solar Orbiter mission has a payload of ten in situ and remote sensing instruments. The in situ instruments include an Energetic Particle Detector (EPD; Rodríguez-Pacheco et al. (2020)), Magnetometer (MAG; Horbury et al. (2020)), Radio and Plasma Waves Instrument (RPW; Maksimovic et al. (2021)), and Solar Wind Analyzer (SWA; Owen et al. (2020)). We use Level 2 (science calibrated) DC magnetic field measurements from the magnetometer; and particle and heavy ion measurements from the SWA suite. The DC magnetic field measurements are in RTN coordinates, like the PSP magnetometer measurements. The SWA suite takes high cadence measurements of heavy ion abundances and 3D VDFs of electrons, protons, and alpha particles. The combination of sensors allows for the characterization of the ion and electron bulk properties of the solar wind between 0.28 and 1 AU (Owen et al. 2020). The Heavy Ion Sensor (SWA/HIS; Livi et al. (2023)) determines abundances of heavy ions, which allows us to determine elemental composition and charge state ratios of the plasma, key measurements not available with PSP. Heavy ion measurements such as Fe/O, O⁷⁺/O⁶⁺, and C⁶⁺/C⁴⁺ ratios are a Level 3 data product from SWA/HIS with a resolution time of 10 minutes (Owen et al. 2020; Livi et al. 2023). Using SWA/PAS, we take measured proton fluxes and velocities at a 4-second cadence to characterize the bulk plasma properties of the solar wind. All Solar Orbiter data used in this study can be found on the Solar Orbiter Archive ³.

In addition to in situ measurements from PSP and Solar Orbiter, we use magnetograms from SDO/HMI and GONG as inputs to our modeling methods (described in Section 3). GONG provides full-disk magnetograms every minute with a resolution of 5 arc seconds, which are publicly available through the NSO website ⁴. HMI provides full-disk Doppler velocity measurements, line of sight photospheric magnetic flux, and continuum images at one arc second resolution with a 45-second cadence along with vector magnetic field measurements at 90 or 135-second cadence (Scherrer et al. 2012). These measurements are produced with the 6177.3nm Fe I line with a resolution of 0.5 arc seconds per pixel, and the solar disk fills almost the entire image frame in HMI data. In addition to HMI, SDO has the Atmospheric Imaging Assembly (AIA; Lemen et al. (2012)), which provides high-resolution full-disk images of the solar corona and transition region at a 12-second resolution. AIA consists of four telescopes taking images at a variety of wavelengths. To produce high-resolution, full-Sun Carrington EUV maps for comparison with models, we use images from the Fe XII (193 Å) bandpass filter aboard SDO/AIA. All SDO/HMI and SDO/AIA data can be accessed through JSOC ⁵.

In order to carry out a conjunction study using PSP and Solar Orbiter data, we are interested in time periods when both spacecraft are observing the same plasma. These time periods are those when the spacecraft is aligned along a Parker spiral streamline, or measuring the same magnetic footpoint longitude in Carrington coordinates, and ideally at similar latitudes. We identify periods of alignment by mapping the latitude and longitude of the spacecraft’s orbit down to a few solar radii. Panel (c) in Figure 1 shows the position of the spacecraft during the perihelion of E11 and their Parker spiral alignment. This time period is ideal for a case study as measurements for all quantities needed in this study were available, and we cross a variety of solar magnetic structures during the spacecraft’s trajectory. Rivera et al. (Submitted) show evidence of this conjunction for part of this interval through four methods: matching

¹ <https://fields.ssl.berkeley.edu/data/>

² <http://sweap.cfa.harvard.edu/Data.html>

³ <https://soar.esac.esa.int/soar/>

⁴ <https://gong.nso.edu/>

⁵ <http://jsoc.stanford.edu/>

magnetic field polarities, mapping velocity peaks to the same longitudes, and matching helium abundance and mass flux between the spacecraft.

In order to directly compare measurements between PSP and Solar Orbiter, we plot the observations as a function of projected longitude using ballistic propagation (Figure 1). [Snyder & Neugebauer \(1966\)](#) first proposed this method of connecting an ideal Parker spiral field line from a point in the heliosphere to the corona, assuming a constant solar wind speed. [Nolte & Roelof \(1973\)](#) demonstrated the capabilities of this method to provide a reliable estimate of solar surface footpoints. While this technique does not accurately represent the real solar wind, which has a non-constant speed; [Nolte & Roelof \(1973\)](#); [Macneil et al. \(2022\)](#); [Koukras et al. \(2022\)](#) estimates the error to be less than 10° in longitude as the two corrections, coronal corotation and solar wind acceleration, cancel to first order. We propagate field lines inward from their initial position in the PSP and Solar Orbiter trajectory to their associated latitude and longitude on the source surface at $2.0R_\odot$ using a varying solar wind speed (the in situ v_R measurement) to most accurately represent the real solar wind following [Badman et al. \(2020\)](#) equation (1). This allows for direct comparison of observations as a function of source longitude.

In Figure 1, we show the mapped in situ data and classification of our regions of interest shaded as follows: blue (HCS crossing), pink (FSW), purple (SASW), green (SSW). Wind is classified as fast or slow using the Solar Orbiter velocity measurement with the 500 km s^{-1} cutoff (panel (b)), and we identify regions of high (or low) Alfvénicity by looking at the absolute cross helicity ($|\sigma_C|$) and residual energy ($|\sigma_R|$) as defined in Equations 1 and 2 (panel (a)). $|\sigma_C|$ is a proxy for the Alfvénicity of the plasma where higher cross helicity measurements ($|\sigma_C|$ values of 1 or -1) are indicative of pure Alfvén waves propagating parallel or antiparallel to the magnetic field. Plasma is considered to have high (or low) Alfvénicity when $|\sigma_C|$ is above (or below) 0.9, while the residual energy tells us the difference between the energy in velocity and magnetic field fluctuations and which is dominant in the plasma.

$$\sigma_C = \frac{\langle E^+ \rangle - \langle E^- \rangle}{\langle E^+ \rangle + \langle E^- \rangle} \quad (1)$$

$$\sigma_R = \frac{2 \langle z^+ \cdot z^- \rangle}{\langle E^+ \rangle + \langle E^- \rangle} \quad (2)$$

In these calculations, $\langle \dots \rangle$ corresponds to a time average over a 20-minute non-overlapping time window, a timescale typical of Alfvénic fluctuations ([Tu & Marsch 1995](#)). E^\pm is the energy ($E^\pm = |(z^\pm)^2|$) of the Elsässer ([Elsässer 1950](#)) variables $\mathbf{z}^\pm = \delta\mathbf{v} \pm \delta\mathbf{B}/\sqrt{\mu_0 m_p N_p}$ ([Wicks et al. 2013](#); [Chen et al. 2013](#)) where $\delta\mathbf{v}$ and $\delta\mathbf{B}$ are the fluctuations of velocity and magnetic field. We use a standard method to validate our cross helicity results in Figure 8 in the Appendix (Section 8) by showing the circular shape (as expected) within a radius of 1 of the σ_C versus σ_R (residual energy) plot ([Bavassano et al. 1998](#)) and further discuss the degradation of the cross helicity calculation between PSP and Solar Orbiter, showing the necessity of PSP measurements to use this quantity as a classifier. Panel (c) is the scaled radial magnetic field showing flux conservation and the HCS alignment achieved through ballistic propagation. Panel (d) shows the source surface heliographic longitude and latitude, highlighting that the latitudes were nearly identical (a rare occurrence) and that the spacecraft moved over structures in the opposite direction.

We show the full set of the data of interest in Figure 2 as a timeseries of PSP (left column) and Solar Orbiter (right column) measurements: velocity (panels (a) and (f)), scaled proton density (panels (b) and (g)), and scaled radial magnetic field (panels (c) and (h)). Both proton density and magnetic field are scaled by R^2 for the time period of interest. Panels (d) and (i) show the cross helicity ($|\sigma_C|$) as calculated for both PSP and Solar Orbiter. We see the measurement from Solar Orbiter does not allow us to characterize the Alfvénicity of the plasma properly, due to a lack of data and the decoherence of the cross helicity measurement with radial distance. Panel (e) shows the Mach number (M_A) from PSP while panel (j) shows the SWA/HIS Fe/O ratio normalized to its photospheric abundance (0.0589) from ([Asplund et al. 2021](#)), a strong tracer of the source region. The Alfvénic Mach number the ratio of the bulk solar wind velocity to the Alfvén speed ($M_A = v_R/v_A$). Periods with M_A below 1 are considered sub-Alfvénic. For this study, we use all the PSP data shown along with the measurements from SWA/HIS on Solar Orbiter and use our ballistic mapping results (Figure 1) to track the mapped features in the timeseries.

3. CORONAL MODELING

We extend the backmapped spacecraft locations of the PSP and Solar Orbiter measurements all the way to their estimated photospheric footpoints with PFSS and MHD modeling. We use and compare these modeling methods to each other to provide confidence in our backmapping and footpoint estimations. By comparing these results to several

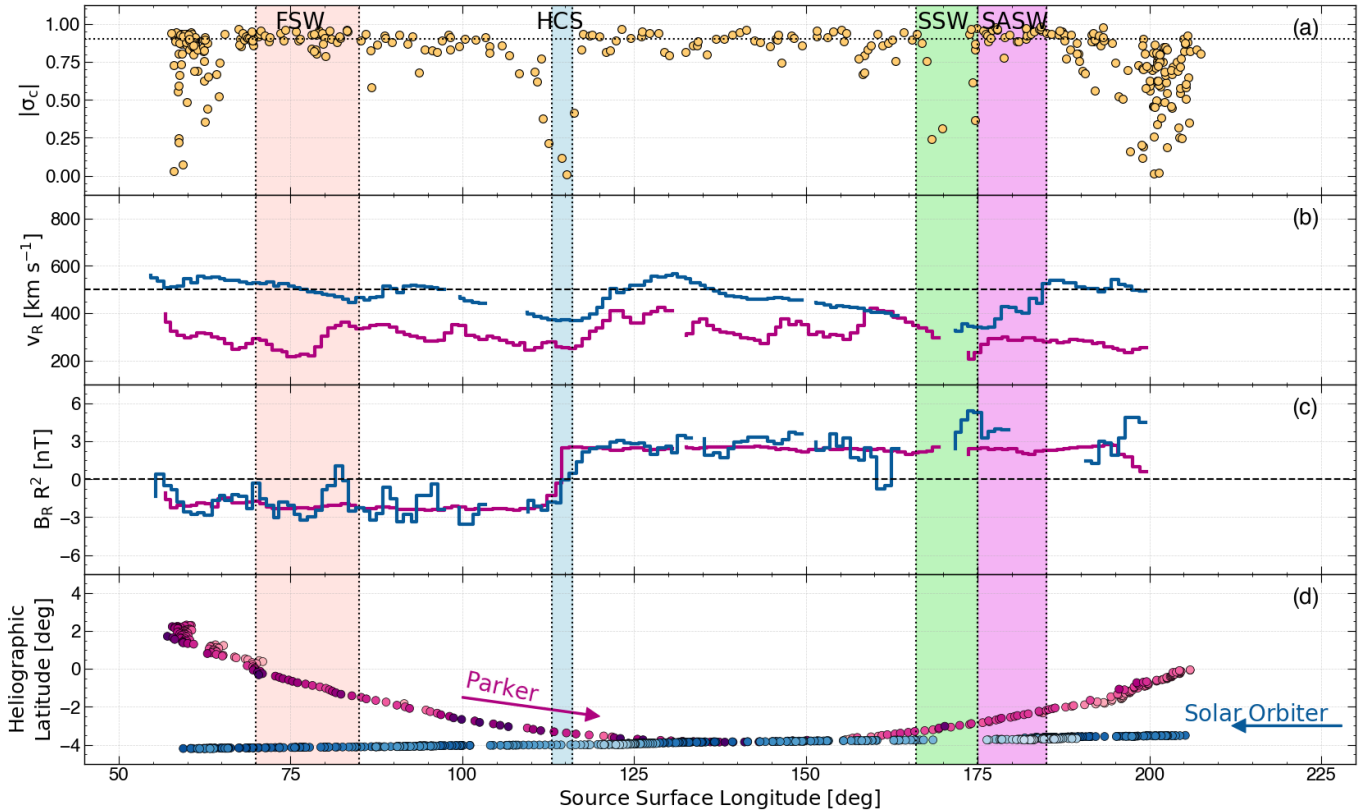


Figure 1. Parker spiral alignment between PSP and Solar Orbiter during PSP E11 showing identification of regions of interest to this study. The HCS in blue, FSW in pink, SSW in green, and SASW in purple. *Panel (a):* Absolute cross helicity (an Alfvénicity proxy) as calculated from PSP measurements and outlined in Equation 1. The dashed line at 0.9 shows the cutoff between Alfvénic and non-Alfvénic wind. *Panel (b):* Comparison of radial velocity as measured by PSP (pink) and Solar Orbiter (blue). The dashed line shows the canonical 500 km s^{-1} cutoff between fast and slow wind at 1AU. *Panel (c):* The scaled radial magnetic field as measured by PSP (pink) and Solar Orbiter (blue) shows the alignment of the HCS crossings and the conservation of flux. The dashed line at 0 shows where the spacecraft crossed the neutral line. Velocity and magnetic field measurements are in 1° longitude bins. *Panel (d):* The trajectories of PSP and Solar Orbiter, in heliographic longitude and latitude, showing the direction of travel and the Parker spiral alignment during this time period. Points are colored by the average solar wind speed in each 1° longitude bin.

in situ data constraints we evaluate this mapping, learn more about the plasma properties of the source regions and how they evolve from PSP to Solar Orbiter (~ 10 to $\sim 120 R_\odot$). Both methods are described below.

3.1. Potential Field Source Surface Modeling

In this work, we use the PFSS model along with an ideal Parker spiral to estimate the photospheric footpoints of the plasma of interest. The PFSS model is an extremely computationally effective method for the determination of the large-scale features of the global coronal magnetic field, typically producing results that compare well with more sophisticated models (Riley et al. 2006; Badman et al. 2023). This modeling allows for the prediction of results from in situ measurements, and the potential to understand many of the outstanding questions in plasma physics such as coronal heating, and solar wind origins (e.g. Badman et al. 2020).

The PFSS model assumes a magnetostatic (current-free) corona with an inner boundary of direct photospheric magnetograph observations of the radial magnetic field (Schatten et al. 1969; Altschuler & Newkirk 1969) and an outer boundary as an equipotential surface where magnetic field lines are assumed to be open and purely radial such that plasma can escape. This outer boundary has a canonical value of $2.5 R_\odot$ (Hoeksema 1984).

We create PFSS models using the `pfsspy` package, an open-source Python package for Potential Field Source Surface Modeling (Stansby et al. 2020). Using the PFSS modeling method, we trace magnetic field lines from a uniform grid on the photosphere out to the radial source surface. As inputs to the PFSS model, we use synoptic radial magnetic

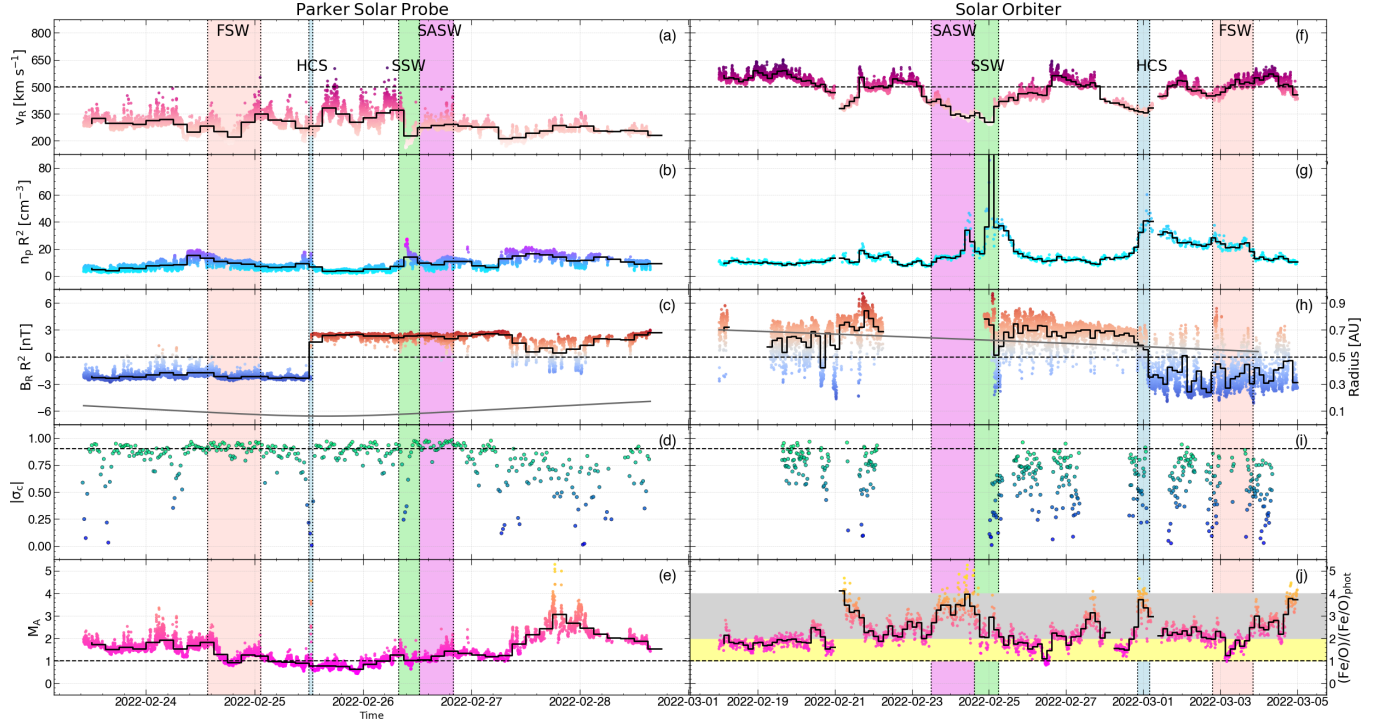


Figure 2. A timeseries showing the data from the period of interest from PSP (left column) and Solar Orbiter (right column). The top panels (panels (a) and (f)) show the solar wind velocity (km s^{-1}), the second panels (panels (b) and (g)) show scaled proton density (cm^{-3}), and the third panels (panels (c) and (h)) show the scaled radial magnetic field (nT). We also show the radial position of the spacecraft in AU (grey) in panels (c) and (h) alongside the scaled radial magnetic field. In Panels (d) and (i), we show the absolute cross helicity ($|\sigma_c|$) as measured by PSP and Solar Orbiter, along with a dashed line at 0.9 showing the cutoff between Alfvénic and non-Alfvénic wind. The bottom panel in the PSP column (panel (e)) shows the Alfvén Mach number and periods below one are considered sub-Alfvénic. Panel (j) shows the $(\text{Fe}/\text{O})/(\text{Fe}/\text{O})_{\text{phot}}$ as measured by the SWA/HIS instrument aboard Solar Orbiter. This panel is shaded in yellow to show ratios between 1 and 2 (typical of coronal hole wind) and grey to show regions between 2 and 4 (typical of other types of wind). The velocity panels (panels (a) and (f)) include a dashed horizontal line at 500 km s^{-1} showing the canonical cutoff between fast and slow wind, and the magnetic field data (panels (c) and (h)) has a horizontal dashed line at the neutral point. The data is overlaid with binned data (3-hour cadence) in black. We highlight the regions of interest in time as corresponding to the longitudinal spans highlighted in Figure 1. These regions correspond to the same position in source surface longitude for both spacecraft when using ballistic propagation to map between the locations of the two spacecraft, but correspond to different periods and lengths of time for PSP and Solar Orbiter due to variances in the direction and speeds of the trajectories.

field maps and a value for the source surface height at which the field is set to be fully radial (R_{ss}). The `pfsspy` package creates a full 3D magnetic field within this low coronal domain along with the ability to trace individual field lines from a photospheric footprint.

For the input synoptic radial magnetic field map, we use magnetograms produced using the Air Force Data Assimilative Photospheric Flux Transport (ADAPT; Worden & Harvey (2000); Arge et al. (2010, 2011, 2013); Hickmann et al. (2015)) model. This model uses flux transport processes to create a more accurate picture of the global photospheric magnetic field by modeling far-side evolution. ADAPT magnetograms are produced using magnetograms from both HMI and GONG. In this work, we use ADAPT-GONG magnetograms downloaded from the National Solar Observatory (NSO) archive⁶ and choose a radial source surface height of $2.0 R_{\odot}$ to complete the PFSS boundary conditions. This is determined to be the optimal value by varying the source surface height until we find the strongest matching between modeled and detected coronal holes and between the modeled and observed HCS (Badman et al. 2022). This modeling traces magnetic field lines between the source surface at $2.0 R_{\odot}$ and the solar photosphere, but PSP and Solar Orbiter make measurements around $13.3 R_{\odot}$ and $120 R_{\odot}$ respectively during this time period. To fill

⁶ <https://gong.nso.edu/adapt/maps>

this gap, we use a ballistic propagation model as discussed in Section 2 to propagate field lines inward and connect the spacecraft trajectories to the PFSS model. This combination then allows us to estimate the photospheric footpoints from which the plasma emerged. We show a comparison of footpoint estimations for varying source surface heights in panel (d) of Figure 3, with the black footpoints ($2.0 R_{\odot}$) as the footpoints we use for this study. In Appendix 9, we vary the velocity used for ballistic propagation by $\pm 10 \text{ km s}^{-1}$ and the source surface location of PSP by $\pm 5^{\circ}$ to understand how small errors in propagation can effect our estimated footpoints. We find that variance in both source surface height and inducing small errors into the ballistic propagation do not change the resulting source region of the observed wind.

3.2. Magnetohydrodynamic Models

In addition to our PFSS modeling technique, we use an MHD model to compare with and validate our PFSS results. The MHD equations are a set of coupled differential equations for large-scale electrically conducting fluids. We use the Predictive Science Inc. (PSI) Magnetohydrodynamic Algorithm outside a Sphere (MAS) code to solve the MHD equations on a non-uniform mesh grid (Riley et al. 2021)⁸. The MAS code is driven by an observed photospheric radial magnetic field measurement from either SDO/HMI or GONG as an inner boundary condition for the solar magnetic field at $1 R_{\odot}$ and a heating mechanism. In this paper, we use the semi-empirical thermodynamic solution (Lionello et al. 2001, 2008), which solves the MHD equations with empirical thermodynamic approximations of energy transport. MAS models are run on two regimes, the coronal regime from $1 R_{\odot}$ to $30 R_{\odot}$ and the heliospheric regime from $30 R_{\odot}$ out to 1 AU , which improves the efficiency of the computation. The model calculates observables such as velocity, density, and radial magnetic field, which can be compared with in situ and ground-based observations.

In order to directly compare the measured observables to the model, we sample the MHD modeled observables of interest at PSP's location *in 3D* for the full trajectory (Figure 3) and compare with the radial magnetic field, density, and velocity measurements from PSP which are taken fully within the coronal model regime. A full Carrington map of the radial cuts of the magnetic field, density, and velocity observables compared with in-situ measurements can be found in the Appendix (see Section 9 Figure 9). We find very good agreement between the measured and modeled observables, validating that our model is properly functioning and is usable to trace magnetic field lines and estimate photospheric footpoints. In Figure 3, we show the correlation between the PFSS and MHD estimated footpoints: 0.998 in longitude and 0.617 in latitude for our chosen model with a source surface height of $2.0 R_{\odot}$. The MHD tracing has no assumptions of ballistic propagation or source surface height and thus provides a strong comparison point with our estimated PFSS footpoints. This, coupled with the strength of the MHD model in reproducing measured plasma parameters, allows for confidence in the footpoints as estimated via the PFSS and MHD models.

4. OBSERVATIONS AND DISCUSSION

We combine data from both PSP and Solar Orbiter during PSP E11 with modeling results to understand the origins of the SSW and SASW. In Figure 2, we see that both spacecraft had sharp HCS crossings that map very close to each other (Figure 1) while traveling in opposite directions in the solar corotating frame: PSP on February 25, 2022 and Solar Orbiter on March 1, 2022. The HCS crossing is sharper in the PSP measurements as PSP moves at a much larger tangential speed than Solar Orbiter.

We use ballistic mapping to map the observed plasma back to the source surface and plot the data as a function of Carrington longitude rather than as a timeseries. This allows us to more easily directly compare structures observed by both spacecraft and relate SWA/HIS composition measurements to PSP in situ signatures. In this section, we outline the observations and discuss their implications in determining the source regions of the solar wind.

4.1. Heavy Ion and Elemental Composition Signatures

In situ elemental composition measurements can be used to connect heliospheric structures to their solar origin by comparing them to characteristic elemental abundances of coronal sources. Similarly, ion composition reflects characteristics of the source region's thermal structure, as well as the properties of its thermodynamic evolution. By combining the elemental composition and charge state measurements from Solar Orbiter (measurements PSP does not provide) with PSP measurements close to the Sun, which degrade with radial distance (such as Alfvénicity), we can more effectively relate heliospheric structure to their coronal sources.

⁸ <https://www.preds-ci.com/mhdweb/home.php>

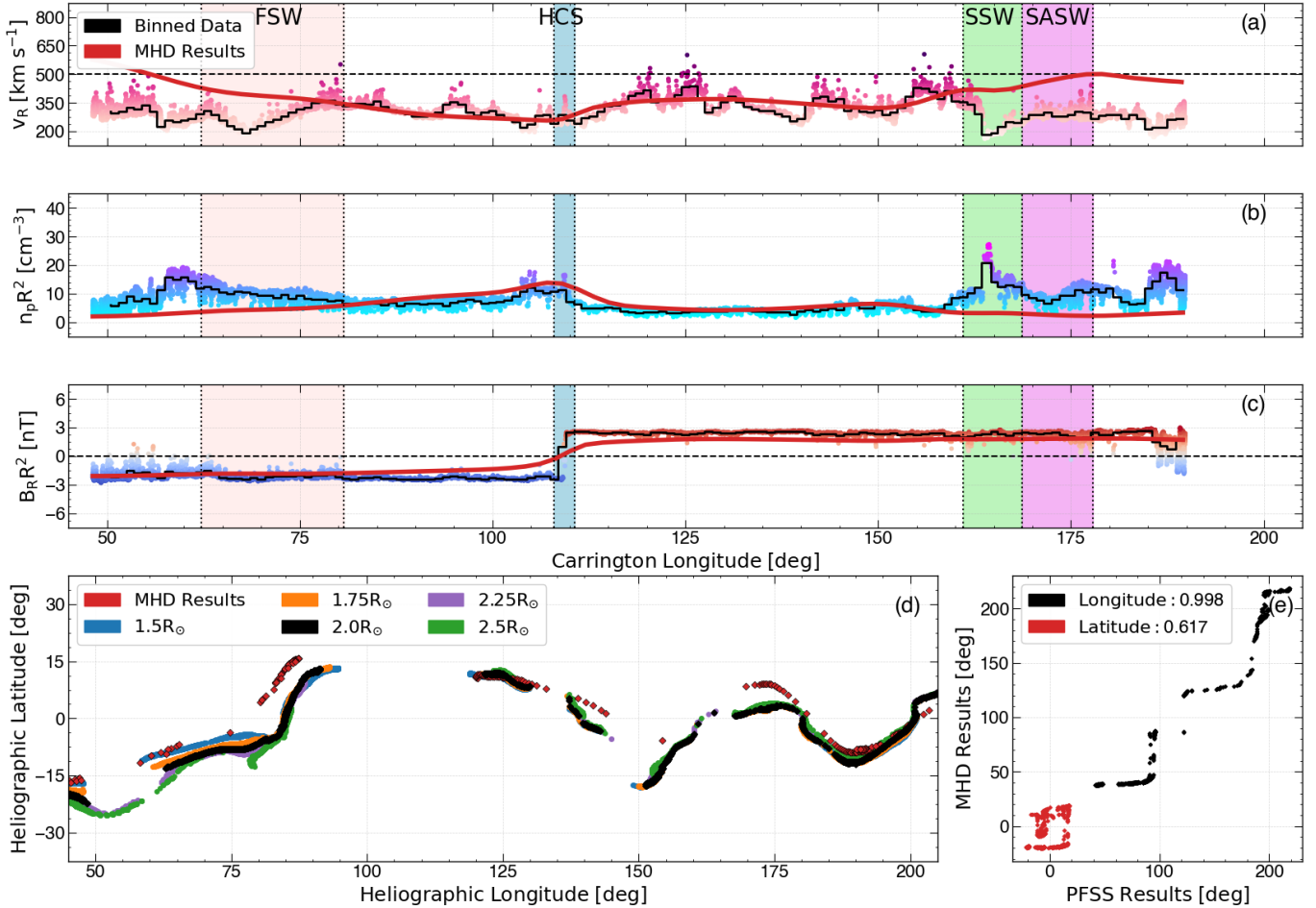


Figure 3. MHD model produced with the PSI MAS code (Riley et al. 2021) for PSP E11 using a SDO/HMI magnetogram from February 24, 2022 as the input boundary condition. The top three panels compare the observables as modeled by the coronal MHD solution (red) at the location of PSP throughout its trajectory, with in-situ measurements of the same parameters from PSP. We show the raw data from PSP overlaid with data binned by 1 degree in longitude (black). *Panel (a):* Comparison between modeled and in-situ radial proton velocity. *Panel (b):* Comparison between the scaled proton density from the MHD model and the PSP measurement. *Panel (c):* Modeled scaled radial magnetic field (red) compared with the measured scaled radial field (black). *Panel (d):* Comparison of the photospheric footpoints between the MHD (red) and PFSS model solutions. We show estimated footpoints from PFSS models at different R_{ss} heights. *Panel (e):* The correlation between the two models with coefficients of 0.99 and 0.62 for longitude and latitude, respectively.

As seen in Figure 4, the ion (C^{6+}/C^{4+} , O^{7+}/O^{6+}) and elemental (Fe/O) composition measurements vary greatly over the time period of interest. The Fe/O ratio in panel (a) is scaled to its photospheric value according to $((Fe/O)/(Fe/O)_{phot})$ where $(Fe/O)_{phot} = 0.0589$ (Asplund et al. 2021). From this point on, discussion of the Fe/O ratio will refer to the normalized $((Fe/O)/(Fe/O)_{phot})$ value. The normalized Fe/O ratio has been shown to relate to coronal source region properties and alongside modeling is a good tracer of solar wind source. The yellow-shaded region shows ratios between 1 and 2 (photosphere-like composition typical of CH regions) while the grey region covers ratios from 2 to 4 (coronal-like composition typical of non-CH wind). Similarly, the ion charge state ratios in panel (b) are a diagnostic of a coronal temperature, allowing us to probe the thermal properties of the stream’s coronal source. We include a dashed line in panel (b) at 0.145 which is the cutoff for the O^{7+}/O^{6+} ratio from Wang (2016) between streamer (high O^{7+}/O^{6+}) and CH wind.

We see variance in the Fe/O ratio, which implies a combination of source regions for the plasma that is measured throughout the encounter. We primarily see ratios ranging between 2 and 4, which is usually the case for active region outflow as found in Feldman & Laming (2000); Widing & Feldman (2001). Similar to the Fe/O ratio, ion charge state ratios provide a key tracer of the plasma the spacecraft is measuring, indicating the electron temperature and density

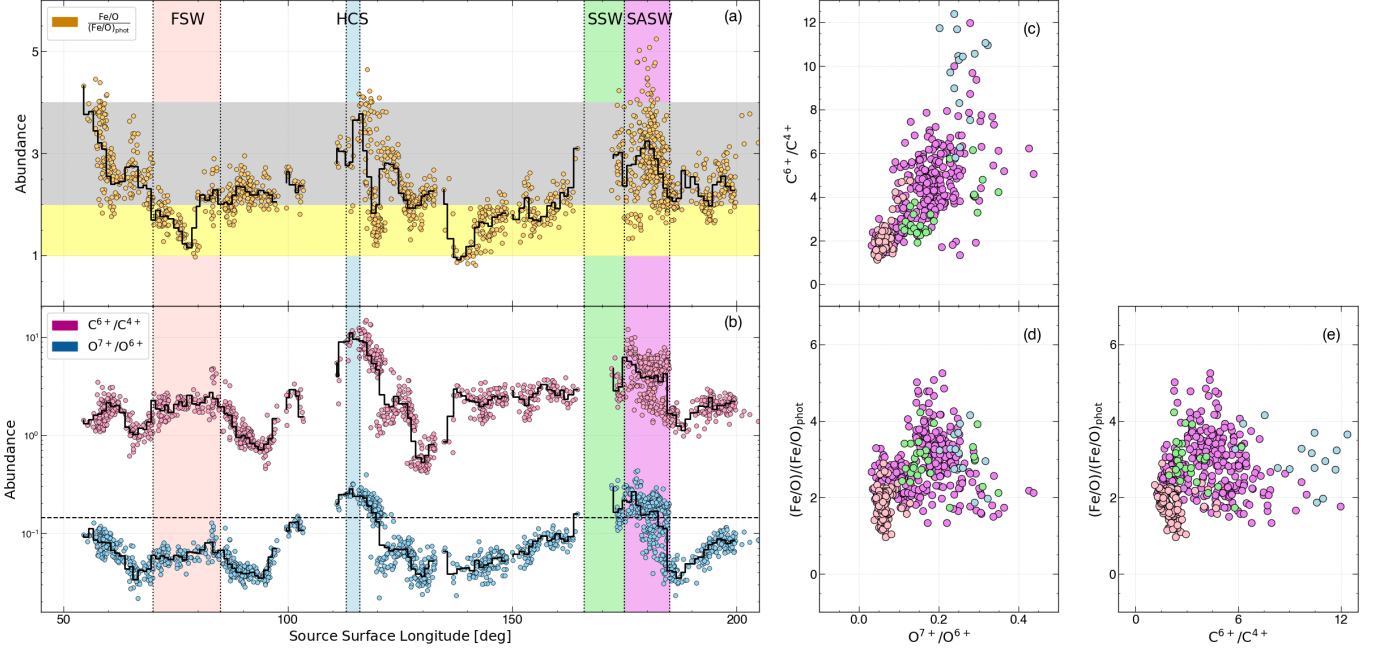


Figure 4. Panel (a): The normalized Fe/O ratio as per Asplund et al. (2021) as a function of source surface longitude. We shade regions where the abundance ratios are between 1 and 2 in yellow, and between 2 and 4 in grey. We overplot the raw data with binned data at a 1° longitude cadence. Panel (b): Ion charge state ratios from SWA/HIS overplotted with 1° in longitude binned data. We include a dashed vertical line at 0.145, which is shown to be the threshold for the O^{7+}/O^{6+} ratio separating coronal hole wind from streamer wind (Wang 2016). Panels (c), (d), and (e): Comparison between O^{7+}/O^{6+} and C^{6+}/C^{4+} , O^{7+}/O^{6+} and Fe/O, and C^{6+}/C^{4+} and Fe/O ratios respectively for the regions of interest. Correlations for each wind regime can be found in Table 1. The colors of each data point correspond to the color for each regime as in panels (a) and (b).

along the path the plasma parcel took through the corona. The majority of this time period consists of low C^{6+}/C^{4+} and O^{7+}/O^{6+} ratios, which imply a low characteristic electron source temperature. Throughout the encounter, the O^{7+}/O^{6+} ratio varies between 0.022 and 0.44, while the C^{6+}/C^{4+} ratio shows a far wider variance between 0.42 and 14.9. The Fe/O ratio ranges between 0.80 and 5.25 for this time period.

In panels (c), (d), and (e) of Figure 4 and in Table 1, we investigate the correlations between the charge state and elemental abundance ratios. The data points are colorized according to the time interval of interest shown in the left-hand panel. The ion ratios (C^{6+}/C^{4+} and O^{7+}/O^{6+}) are strongly correlated with each other, with a Spearman correlation coefficient of 0.78, but not with the Fe/O ratio (Figure 4). Both the C^{6+}/C^{4+} and O^{7+}/O^{6+} ratios are indicators of electron temperature with some radial evolution effects and as such, are expected to follow the same trends as they have similar freeze-in heights (Zhao et al. 2017). The C^{6+}/C^{4+} and O^{7+}/O^{6+} ratios have Spearman correlation coefficients of 0.15 and 0.33 with Fe/O, respectively. The lack of overall correlation between the charge state ratios and elemental composition implies the presence of a variety of solar wind sources. There has not been a strong correlation observed between Fe/O and solar wind speed as seen by both SWA/HIS and ACE/SWICS (Livi et al. 2023) and so we would not necessarily expect a strong correlation with the charge state ratios and Fe/O. This could be because the characteristic source region temperature can be transient in nature (heating and cooling occurring at noticeable timescales) while the FIP effect takes place on a longer timescale, or the outflow effects are important – the density, temperature, and bulk speed that set the ion ratios during outflow varies across source regions with similar Fe/O.

When looking at the correlations for the different time periods of interest, we see some distinct groupings. The FSW typically shows far lower ion ratios than the other types of wind, especially when compared to the SSW and HCS wind. It shows a strong correlation between O^{7+}/O^{6+} and C^{6+}/C^{4+} but a low negative correlation between the ion ratios and Fe/O. The SSW shows some correlation between the ion ratios, almost no correlation between O^{7+}/O^{6+} and Fe/O and a low negative correlation for C^{6+}/C^{4+} and Fe/O. Similar to the FSW, the SASW has a higher correlation between the charge state ratios. Looking at the correlation plots, we see two groups of SASW, most distinct in panel (c). In all three panels, there is a lower left blob of points more similar to FSW-like characteristics and an upper

right blob of points found almost between the HCS and SSW blobs. The SSW also shows some grouping that is found mainly at the inner boundary between the SASW blobs with some points closer to the HCS plasma, while the HCS grouping is on the outer right edge of the SASW group. Similar to Zhao et al. (2017); Rivera et al. (2021), we see some of this characteristic ‘Outlier’ SSW in panel (c) of Figure 4 where the C^{6+}/C^{4+} ratio is much lower than expected in comparison to the O^{7+}/O^{6+} ratio. This is slow wind thought to have streamer or active region origins and is strongly correlated with the solar cycle (Rivera et al. 2021).

Wind Type	O^{7+}/O^{6+} vs. C^{6+}/C^{4+}	O^{7+}/O^{6+} vs. Fe/O	C^{6+}/C^{4+} vs. Fe/O
All	0.78	0.33	0.15
HCS	0.43	-0.38	-0.45
FSW	0.85	-0.27	-0.19
SSW	0.50	0.012	-0.27
SASW	0.66	0.19	-0.03

Table 1. Spearman correlation coefficients between charge state ratios (O^{7+}/O^{6+} and C^{6+}/C^{4+}) and Fe/O, a measure of the low FIP bias in the solar wind. We show the correlation for each type of wind along with the correlation for the entire time period.

The largest change in the C^{6+}/C^{4+} and O^{7+}/O^{6+} ratios occurs at the current sheet crossing, where plasma tends to be slow, dense, and hot, which allows more time for ionization thus producing higher abundances of O^{7+} and C^{6+} . These sharp increases in ionization state of these species indicate regions of increased coronal electron temperatures. This is a common effect when crossing the HCS and provides a validation metric for comparing our modeling methods with observations. In this encounter, we see an increase of 608% in the C^{6+}/C^{4+} abundances, 130% in the O^{7+}/O^{6+} abundances, and 113% in the Fe/O ratios over 3° in longitude as we cross the HCS.

In the FSW, we see low O^{7+}/O^{6+} and C^{6+}/C^{4+} ratios during the region, and a dip in these ratios just before and after the regions showing a transition to cooler, less dense coronal hole plasma. The Fe/O ratio during this region has photosphere-like abundance levels with the sharpest dip in the center of the region – indicative of CH type plasma.

The O^{7+}/O^{6+} ratio in the SSW (green) region is well above the threshold of 0.145, implying hot coronal conditions indicative of non-CH origins. There is also a spike in the C^{6+}/C^{4+} ratio at the boundary between the SSW and SASW region implying a pseudostreamer crossing. These composition measurements support our claim that this SSW wind period originates from a pseudostreamer due to the spike in C^{6+}/C^{4+} at the boundary between the Alfvénic and non-Alfvénic SSW and the high ion charge state ratios in this region.

The SASW region has a huge variance in the Fe/O ratio. The ratio increases and decreases through the center of the region indicating some variation in the structure the spacecraft is connected to. Both ion charge state ratios show large variation in this region from more CH-type wind to streamer-like wind. As discussed previously, there seem to be two groupings of composition results for the SASW. This is due to the overlapping in the backmapping in this region, as seen in Figure 1.

4.2. Particle Measurements

The two primary ion components that make up the solar wind are protons and alpha particles, and in this section, we discuss the variance in proton-to-alpha abundance ratio and differential velocity. Similar to the ion ratios discussed in Section 4.1, the alpha particle abundance ratio ($A_{He} = N_\alpha/N_p$) provides insight to identifying the source regions of the solar wind. The relative velocity of alpha particles to protons can vary depending on the type of solar wind and decreases with radial distance from the Sun, and often shows a positive correlation with the bulk solar wind speed (Mostafavi et al. 2022). Despite being more massive, alpha particles have higher velocities than protons close to the Sun (Feldman & Marsch 1997), an example of preferential acceleration at work.

In Figure 5 we show the PSP particle measurements. In panel (a), we show the alpha abundance ratio (A_{He}) and in panel (b) we show the differential velocity normalized by the Alfvén speed ($v_{\alpha p} = \frac{|v_\alpha - v_p|}{v_A}$). In both panels, the color corresponds to the solar wind bulk velocity and the black line shows the data binned by 1° in longitude. We also compare the scaled proton and alpha abundance as a function of wind type in panel (c), using the dashed lines to separate between the high ($A_{He} \geq 0.045$) and low ($A_{He} \leq 0.015$) abundance regimes as defined by Kasper et al.

(2007); Kasper et al. (2012). As in all Figures, we shade the regions of interest and discuss interesting observations below.

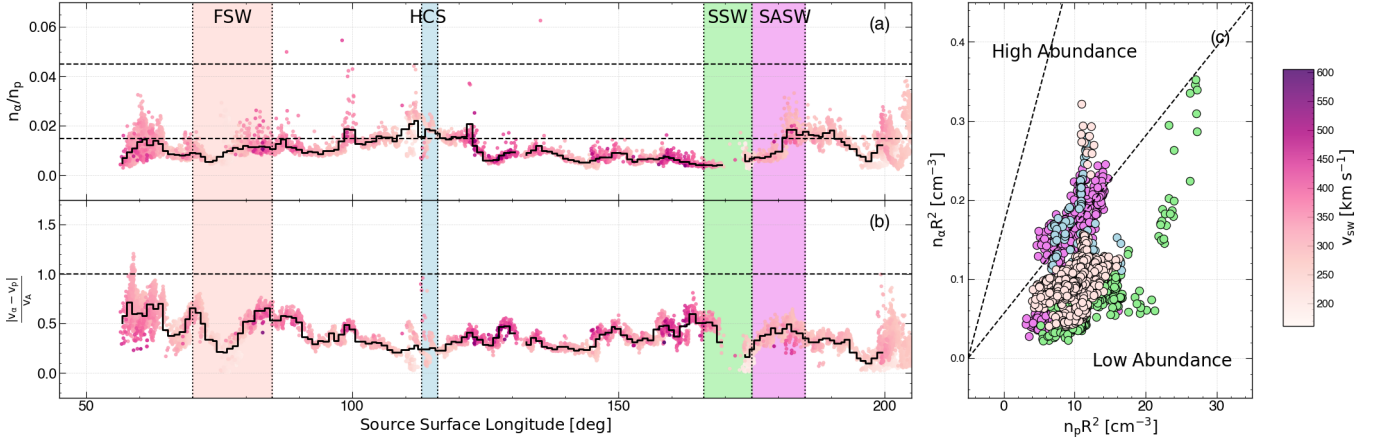


Figure 5. Particle measurements from the SPAN-I instrument aboard PSP/SWEAP showing the alpha-to-proton abundance ratio and velocity differential. *Panel (a):* Alpha-to-proton abundance ratio (n_α/n_p) against source surface longitude. The black line shows the abundance ratio averaged over 1° longitude bins. *Panel (b):* The normalized absolute differential velocity as a function of source surface longitude. 1° longitude binned data is shown by the black line. The dashed horizontal line at 1 separates regimes where the differential velocity is above and below the Alfvén speed. *Panel (c):* The scaled proton density ($n_p R^2$) against the scaled alpha particle density ($n_\alpha R^2$) as a function of the four time periods of interest based on their corresponding colors. In panels (a) and (c), the dashed lines show the high abundance boundary of 0.045 and the low abundance boundary of 0.015. The color scale in panels (a) and (b) corresponds to the bulk solar wind speed measured by PSP as seen on the right.

In Figure 5, we see that overall, the abundance ratio during E11 rarely crosses (and never in the binned data) above the typical ‘high abundance’ threshold of 0.045 (Kasper et al. 2007; Kasper et al. 2012). There is some variance in abundance throughout the encounter, however the ratio remains low for the majority of this period. There is a strong correlation between the proton (v_p) and alpha particle (v_α) bulk velocity with a Spearman correlation of 0.9. The correlation between the differential velocity and the solar wind velocity is weak (correlation of 0.50) and is much stronger between the fast solar wind and differential velocity (0.51) than for the slow wind (0.27). We find that for the entire time frame, the alpha-to-proton differential velocity is below the Alfvén speed, $v_{\alpha p}/v_A$ (panel (b)). This is due to alpha-proton instabilities driving wave-particle interactions to hit the instability threshold, leading to an upper bound on the differential speed of $v_{\alpha p}/v_A \leq 1$ (Gary et al. 2000).

At the HCS crossing, we see an increase in proton density in both the PSP and Solar Orbiter data (Figure 2) along with a dip in helium abundance in panel (b) of Figure 5. There are two clusters of abundance ratios in panel (c): one just above the low abundance threshold and one just below. There is also a wide range of scatter in the differential velocity measurement, with the binned value around 0.25.

In the FSW region, we see both intermediate and very low helium abundances along with differential velocity values ranging between 0.25 and 0.6, and binned values that are higher than in all other regions of interest. In panel (c), we see that the fast wind points fall in the lower left of the plot, similar to the composition data seen in Figure 4. Typically, we expect to see an enhancement in helium abundance in a fast wind regime, which is not the case in the PSP data shown here.

In the SSW region, we see the lowest velocities as measured by PSP (187 km s⁻¹) during this time range and also a sharp dip in the normalized velocity differential with a drop of 97.7%. This drop also corresponds to the lowest helium abundance ratio in the binned data measured throughout this interval (0.004). Low helium abundance wind is characteristic of slow wind from streamers (Kasper et al. 2007), another important piece of evidence for this slow solar wind region to be from a pseudostreamer. In panel (c), we see two groupings of SSW plasma: one with low and one with high proton and alpha densities, both of which are below the low abundance threshold.

The SASW consists of both alpha particle intermediate and poor plasma populations implying that it likely originates from multiple source regions. We can see these two groupings in panel (c) where one group shows more HCS-like abundance ratios, and the other shows more FSW-type ratios.

4.3. Modeling

Using the PFSS and MHD modeling methods, we can estimate the footpoints of the plasma measured in situ by PSP and Solar Orbiter. Our model is able to connect 77% of the observed plasma to a photospheric source footpoint. In Figure 3, we show that the predicted observables (v_{sw} , B_r , N_p) from the MHD model explain the PSP in situ measurements well. This coupled with the strong agreement between the PFSS and MHD footpoint estimation gives us confidence in the location of the photospheric footpoints we use for analysis. In Figure 6, we show the PFSS model for PSP E11 using an ADAPT-GONG magnetogram as the lower boundary input and a source surface height of $2 R_\odot$. We show the modeled HCS along with the footpoints produced using a combination of PFSS modeling and ballistic propagation as described in Section 3.1. PFSS models extract coronal holes through connecting open field lines to their photospheric footpoints. The model allows us to understand the large-scale structure of the corona, showing a vertical HCS warp, negative polarity near equatorial coronal holes to the left of the HCS, and positive polarity near the equatorial holes to the right of the HCS that is consistent with the measured polarity from PSP and Solar Orbiter. The vertical HCS warp was also seen by Liewer et al. (2023) in PSP/WISPR data, providing further validation of our model. The modeled HCS in both the MHD and PFSS models shows great agreement with the measured radial magnetic field polarity from both spacecraft, which suggests that the ballistic propagation method works well and the coronal model is accurate, meaning our footpoints are well estimated.

Figure 6 allows us to understand the large-scale magnetic field configuration during this time period. To better understand the specific source regions of each wind stream, we look at a combination of modeling results. Figure 7 shows the source regions for the three interesting periods. In panels (a) and (b), we overlay the estimated footpoints of the FSW and SASW streams on SDO/AIA images. The images are from a time estimate of when the observed wind left the solar surface, which we calculate using the measured wind speed and the location of the spacecraft. This allows for the strongest comparison with the conditions at the time, such that we are better able to understand the source region.

We see that the FSW (pink footpoints) measured by PSP originates from a coronal hole region around 80° in Carrington longitude. The footpoints at the center of the FSW region are in darker (cooler) coronal plasma, which is consistent with the observation of a dip in the O^{7+}/O^{6+} and C^{6+}/C^{4+} ratios near the fast wind region as seen in Figure 4 which corresponds to lower electron temperatures. The footpoints nicely trace the shape of the CH and provide strong justification that this fast wind stream emerged from an equatorial coronal hole. From Figure 6, we also see low photospheric magnetic field strength and low relative footpoint brightness for this FSW region, both characteristics of wind emerging from CHs. This result also provides additional validation of our footpoint estimations, as it aligns with the expectation for FSW streams.

In Figure 6, we see the first indication that the SSW period came from a streamer crossing – the jump in photospheric footpoints, which indicates the spacecraft crossed a region of closed field connecting two CHs. The background and observed polarity are unipolar, which indicates this is a pseudostreamer rather than a helmet streamer (crossing between two different polarity CHs). In Figure 7, we investigate the connectivity of the SSW stream by taking latitude (panel (c)) and longitude (panel (d)) slices through the 3D MHD solution. The latitude and longitude chosen are shown by the horizontal and vertical dashed lines in Figure 6 respectively. Taking these slices through the model, allows for the determination of the magnetic field configuration around the footpoints of the region, and when used in conjunction with the low expansion factor and slow wind speed indicates that the spacecraft flew through a pseudostreamer during this period (Riley et al. 2015; Wallace et al. 2020). Panel (c) of Figure 7 shows the jump in footpoints (green diamonds) across a closed field region, indicating that the footpoints are connected to the edges of a unipolar streamer. The trajectory of PSP at the source surface ($2.0 R_\odot$) is shown with diamonds that are colored by the measured proton density. We see a narrow density enhancement corresponding to the jump in footpoints in the Carrington frame as PSP crosses the unipolar streamer in both the modeled magnetic field, and in situ B_R observation. In panel (d), we show a longitude slice through the MHD model, where two footpoints (green diamonds) are connected to the edge of a unipolar streamer: one footpoint in front of and one behind the longitude slice. This is because PSP is flying through the plane of the sky during this period. Combining the modeling results, with the in situ observations of a narrow

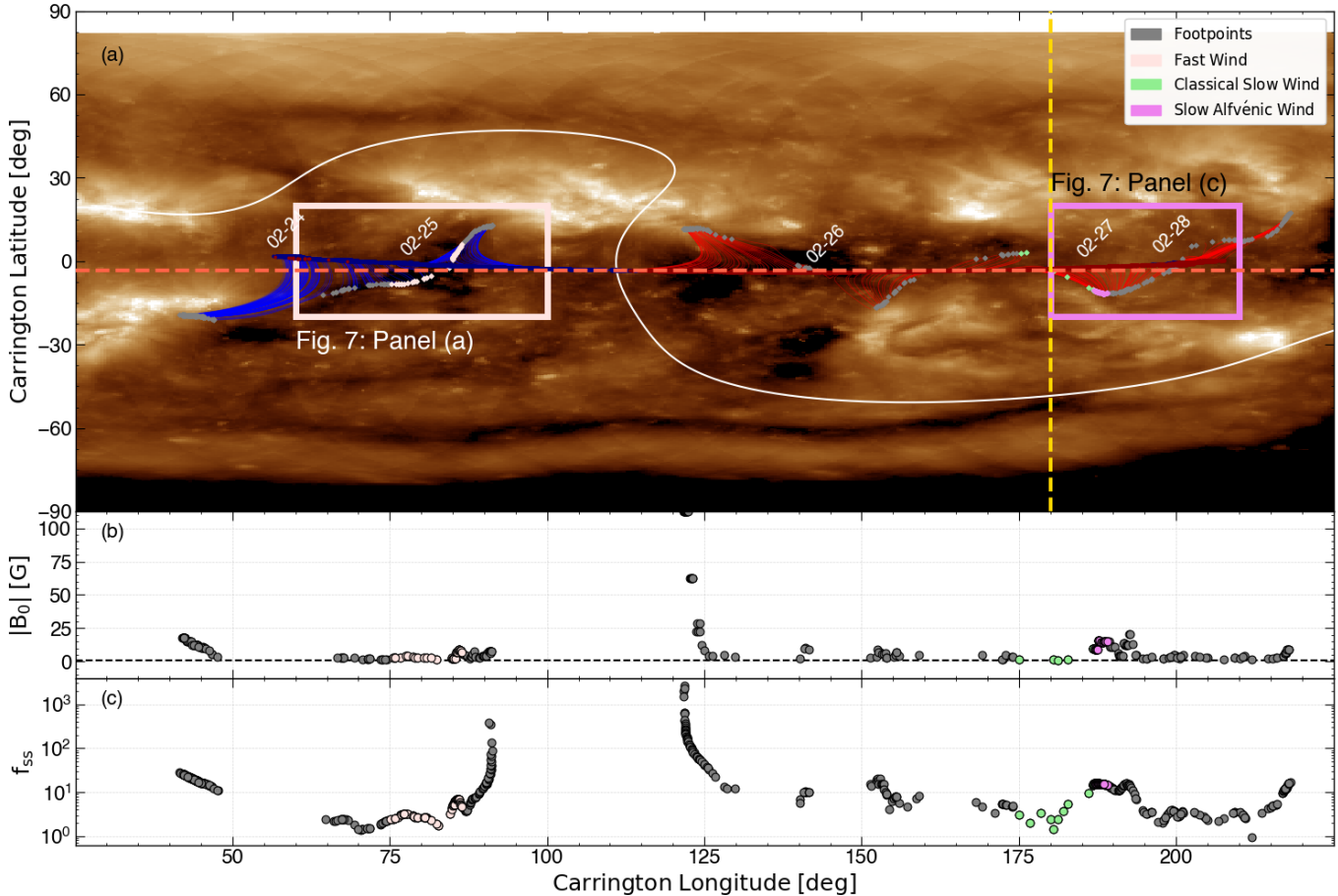


Figure 6. PFSS model for PSP E11 using an input ADAPT-GONG magnetogram from February 24, 2022. *Panel (a):* In this panel, we show a full-Sun Carrington map produced using SDO/AIA 193Å images and overlay the results from our PFSS solution on top. The modeled HCS is in white and the trajectory of the spacecraft is shown colored by the polarity of the magnetic field. The pink and purple rectangles outline the regions of the estimated footpoints of the FSW and SASW, which are shown in more detail in Figure 7. The vertical and horizontal dashed lines correspond to the latitude and longitude cuts we take through the MHD model (Figure 7) to study the connection to the pseudostreamer. *Panel (b):* The absolute photospheric magnetic field strength (G) at the estimated footpoints as a function of longitude. *Panel (c):* The expansion factor calculated following the method of (Wang & Sheeley 1997). In panels (b) and (c) the points for the FSW, SSW, and SASW streams of interest are colored pink, green, and purple, respectively.

density enhancement, drop in speed, uniform polarity and low expansion factor indicate that this SSW stream came from PSP’s crossing of a pseudostreamer structure.

The SASW stream shows some similar properties to the SSW stream and some to the FSW stream. This implies a combination of source regions – the periphery of the pseudostreamer connecting into a positive polarity CH boundary. In panel (b) of Figure 7, we show the SASW stream emerging from the boundary of an equatorial CH. This period has an elevated expansion factor (panel (c) of Figure 6), which is characteristic of wind streaming from the over-expanded pseudostreamer/CH boundary (Panasenco & Velli 2013; Panasenco et al. 2013; Sheeley et al. 2013; Wang 2013; Panasenco et al. 2019).

5. RESULTS

By using a combination of methods, we are able to probe the source regions of the solar wind by connecting models to in situ data. The connection between modeling and in situ data provides insight from both a theoretical and observational point of view as to the origins of the solar wind. While the modeling methods do have user-defined inputs, when combined with in situ observations, they provide strong evidence for source regions of the slow solar wind.

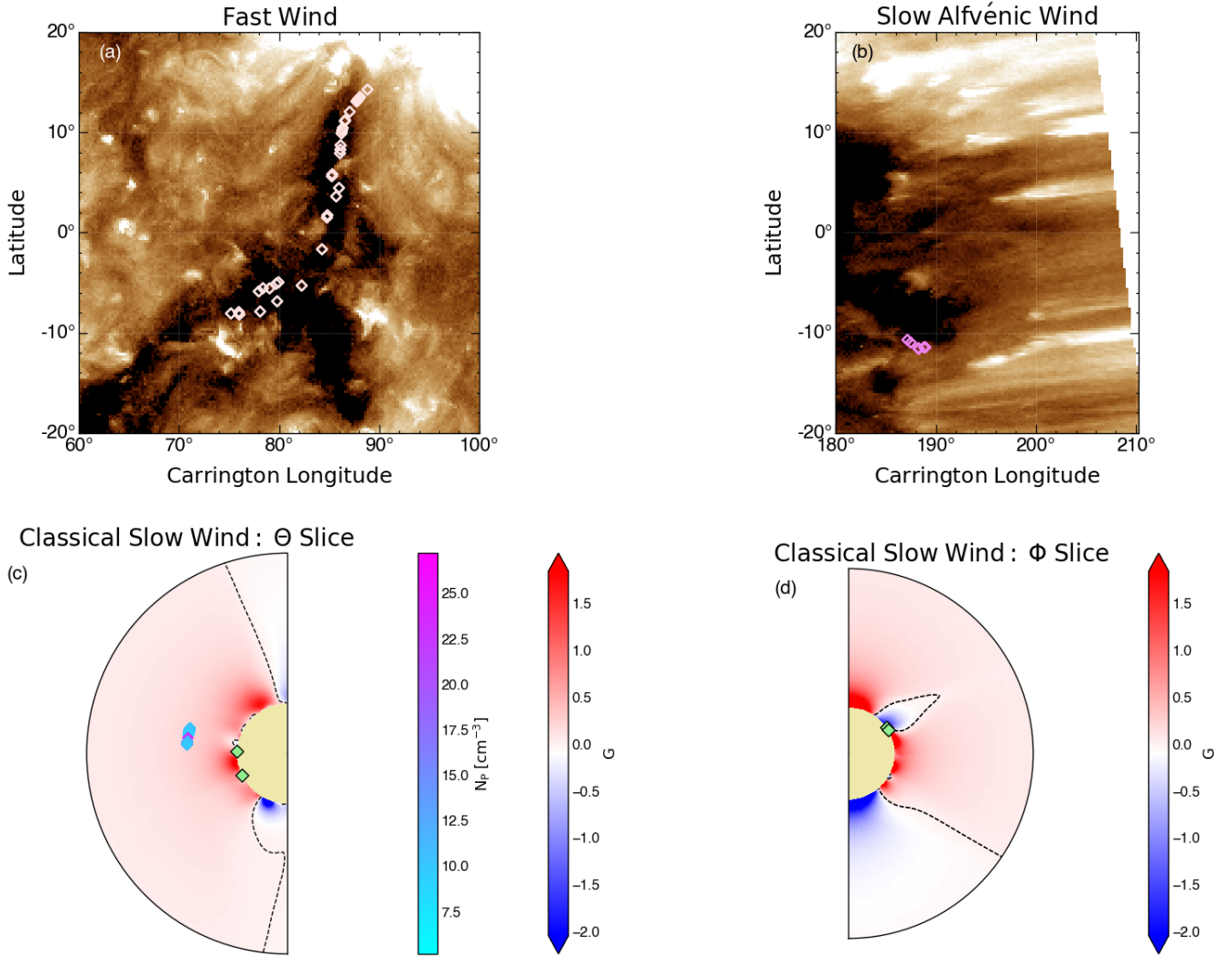


Figure 7. A zoomed in view of the source region connection for the FSW, SSW, and SASW streams of interest. *Panel (a):* Estimated photospheric footpoints for the FSW stream (pink diamonds) overlaid on a SDO/AIA image of the region. This region corresponds to the pink box in panel (a) of Figure 6. *Panel (b):* The estimated photospheric footpoints from the SASW stream (purple diamonds) showing the connection to the edge of a equatorial CH. This region corresponds to the purple box in panel (a) of Figure 6. *Panel (c):* Latitudinal slice through the 3D MHD coronal magnetic field solution (Riley 2021). The slice corresponds to the horizontal red dashed line in panel (a) of Figure 6. The estimated photospheric footpoints of the SSW stream at this latitude are shown with green diamonds. The trajectory of PSP at the source surface ($2.0 R_{\odot}$) is shown with diamonds that are colored by the in situ scaled proton density measurement. The neutral line is shown by a dashed black line. *Panel (d):* Longitudinal slice through the 3D MHD coronal magnetic field solution corresponding to the dashed yellow vertical line in panel (a) of Figure 6. The estimated footpoints at this longitude slice are shown with green diamonds. The neutral line is shown by a dashed black line.

1. Similar to Chen et al. (2021), we see non-Alfvénic slow wind emerging from the HCS supported by an enhancement in the proton density, low alpha-to-proton abundance, and high Fe/O, O^{7+}/O^{6+} , and C^{6+}/C^{4+} ratios.

The in situ measurements of the magnetic field from near the HCS crossing provide observational constraints and validation for our PFSS and MHD models while the composition metrics is typical of plasma in closed coronal loops. HCS plasma typically is slow, dense, and hot where higher O^{7+} and C^{6+} abundances are often observed. The high Fe/O ratio shows strong low-FIP enhancement has taken place in association with closed loop structures in connection to the streamer belt Wang et al. (2000); Howard et al. (2008); Sheeley et al. (2009); Rouillard et al. (2010); Liewer et al. (2023) with helium abundance enhancements near the HCS. We also see

a depletion in the helium abundance ratio near the HCS crossing characteristic of streamers in closed coronal loops. These are all typical in situ metrics for classical non-Alfvénic slow wind.

2. As expected from von Steiger et al. (2000); McComas et al. (1998, 2008), we find that the fast wind stream maps to a relatively large coronal hole region, with low ion charge state ratios and photospheric-like Fe/O abundances, characteristic of coronal hole wind.

As shown in Figure 4, a relatively lower (O^{7+}/O^{6+} and C^{6+}/C^{4+}) ratio in the fast wind stream indicates solar wind originating from a cool CH structure at the Sun. The normalized Fe/O ratios observed in this region fall in the photosphere-like regime, typical of wind emerging from open field lines that has not had the time to fractionate. The modeling results connect the plasma from this region to a large coronal hole with low relative footpoint brightness, providing additional evidence of the source region of the FSW.

3. The slow wind has been shown to have large variation in plasma properties and be associated with the HCS (Antiochos et al. 2011), S-Web (Chitta et al. 2023; Lynch et al. 2023), and pseudostreamers (Wang et al. 2012; Riley & Luhmann 2012). Similar to Wang et al. (2012); Riley & Luhmann (2012), our combination of modeling and in situ measurements show that the SSW region of interest originates from the stalk of a pseudostreamer. We see an enhancement in ion charge state ratios, FIP bias, and proton density around this region, which is typical of streamer wind.

The high Fe/O ratio during this period is indicative of the FIP effect which has been shown to require plasma to be on closed loops and remain in the corona for longer time periods to fractionate (Geiss et al. 1995; von Steiger et al. 2000; Laming 2015). This time period has a spike in proton density, low Alfvénicity in both PSP and Solar Orbiter observations, the lowest helium abundance of the entire time period and a sharp drop in the normalized velocity differential. We also see high ion charge state ratios which implies a high electron temperature of the source region.

The spike in charge state ratios at the boundary between the SSW and SASW regions coupled with the jump in footpoints seen in Figure 6 and density enhancement in both PSP and Solar Orbiter data (Figure 2) without crossing the HCS is indicative that this non-Alfvénic SSW plasma originated from a pseudostreamer stalk.

4. The slow Alfvénic wind during this time period is shown to have two populations of plasma with different characteristics: one that shows more FSW-type characteristics and the other showing more streamer-like properties. Similar to results from D’Amicis et al. (2021), the SASW is thought to originate from an over-expanded pseudostreamer connected to a CH boundary.

The SASW shows coronal-like Fe/O abundance ratios with a spike in the center of the region, showing some variance and perhaps evolution in the structure the spacecraft are magnetically connected to. The ion abundance ratios bound this region with a large range of measured values. The correlation plots show two groupings: one with high charge state ratios and low FIP enhancement and the other with low charge state ratio and photospheric level elemental composition. This regime also shows variance in alpha-to-proton abundance with a grouping similar to the HCS abundance and one similar to the FSW abundance. These groupings along with the modeling results in Figure 6 imply the SASW comes from a pseudostreamer periphery that connects into a positive polarity coronal hole, and the CH boundary itself. Over expansion can occur due to the presence of coronal pseudostreamers, which when coupled with low coronal non-monotonic expansion can slow the solar wind leading to similar properties to the FSW, but much slower wind speeds (Panasenco & Velli 2013; Panasenco et al. 2019; D’Amicis et al. 2021). It is important to note that the neighboring SSW and SASW are difficult to disambiguate in the Solar Orbiter data due to the velocity gradient and ballistic mapping as Solar Orbiter is further from the Sun leading to overlap in the backmapping of these two time periods.

6. CONCLUSION

While the source regions of the slow solar wind still remain an open question, the novel in situ measurements that the new generation of spacecraft, PSP and Solar Orbiter, provide allow us to delve deeper into this question and study the nature of the solar wind. Combining the spacecraft instrumentation via conjunctions allows us to make detailed measurements of the solar wind evolution through comparing quantities known to decohere with radial distance, such as the Alfvénicity, with radially invariant quantities, such as the elemental composition and charge state ratios, which

are fixed in the plasma at low coronal altitudes and therefore utilize the wider range of instrumentation available further from the Sun. In this paper, we outlined the modeling methods and measurements we use to study the coronal source origin of fast and slow solar wind and connect these methods to in situ plasma measurements. With PFSS and MHD modeling, we detect fast wind from deep in coronal holes and that the classical slow solar wind originates from a combination of HCS, pseudostreamer, and active region plasma as found by (Abbo et al. 2016; D’Amicis et al. 2021, and references therein), while the slow Alfvénic solar wind originates from a pseudostreamer stalk connected to a CH boundary. We then look at elemental abundances and particle measurements to study the FIP effect and trace coronal source region. In situ measurements from PSP and Solar Orbiter support our modeling results: fast solar wind has low FIP bias as measured by Fe/O (Figure 4), very low ion charge state ratios implying a relatively cool coronal source, and higher alpha particle abundance ratios in comparison with the slow wind region, characteristic of wind streaming along open field lines from coronal holes. In contrast, slow solar wind shows a variance in density, abundance, and ion ratios implying a combination of source regions. We see both alpha-rich (CH origins) and alpha-poor (active region and/or streamer wind) slow wind and increased ionization states of carbon and oxygen in some slow wind regions, indicating wind from hotter, active region plasma. The Fe/O ratio shows variance in the slow solar wind, oscillating between values characteristic of photospheric and coronal plasma.

In addition to providing evidence towards the source region of the plasma, the in situ measurements provide interesting insight into the plasma escaping from higher in the corona. There is a clear enhancement in charge state ratios and FIP bias as the spacecraft cross the HCS. This characteristic HCS signature seen in the SWA/HIS data shows that we are able to attach composition information to a PSP data set, extending its science potential and capabilities. During this encounter, we uncover a pseudostreamer over which we see an enhancement in the heavy ion ratios and Fe/O (Figure 4) as measured by Solar Orbiter SWA/HIS, a jump in photospheric footpoints, increased proton densities, low Alfvénicity, and no crossing of the HCS. There is also a dip in the velocity differential as we cross this region and the lowest velocities measured during this time frame, supporting the idea of the slow solar wind partially originating from pseudostreamer regions that persists out into the heliosphere as both PSP and Solar Orbiter measured low velocities.

While the combination of modeling methods and novel in situ measurements provide an incomparable insight into the nature and source regions of the solar wind, there is still much work to do to accurately and convincingly determine the source regions of the solar wind (especially the slow solar wind). Modeling methods are limited by the assumptions and input data that we choose to use for our specific study and more work is necessary to create quantitative methods to determine the best input data to use for a model. For example with the PFSS model, the choice of input magnetogram and source surface height drastically impacts the location and shape of the modeled HCS and in situ measurements are required to determine which model most accurately describes the large-scale structure of the coronal magnetic field. These types of models are also hindered by time and spatial evolution of magnetic structures on the solar surface. While the ADAPT flux transport models account for some of the temporal and spatial evolution, there is still more work to be done to create accurate global models of the evolution of the solar surface and more spacecraft to fly to allow for multiple viewpoints of images at once. This conjunction occurred while the source regions were behind the limb, and models would be more robust if we had full-Sun magnetograph coverage.

We see very low alpha abundance in the FSW region and additional exploration of PSP fast wind periods should be done to understand if this is an effect of PSP’s radial position, this encounter specifically, or some other mechanism at work. The slow regions showed a large spread in source properties and coronal conditions for similar solar wind speed, from a priori very similar looking corona, and more work looking at the characteristics of the slow wind in comparison to its Alfvénicity and source region must be done to completely characterize the slow wind and its origination mechanisms. Additionally, further work exploring the impact of source region on wind temperature and the radial evolution of the parameters discussed in this paper (velocity, density, charge state ratios, FIP bias, helium abundance, Alfvénicity, etc.) should be done to fully characterize the solar wind propagating from various source regions. These types of studies require the existence and identification of future multi-spacecraft conjunctions to uncover the effects of radial propagation and have access to a variety of remote and in situ measurements to fully understand the processes at work creating and driving the solar wind.

7. ACKNOWLEDGEMENTS

The FIELDS and SWEAP experiments on the PSP spacecraft was designed and developed under NASA contract NNN06AA01C. PR gratefully acknowledges support from NASA (80NSSC20K0695, 80NSSC20K1285,

80NSSC23K0258), and the Parker Solar Probe WISPR contract NNG11EK11I to NRL (under subcontract N00173-19-C-2003 to PSI).

We acknowledge the NASA Parker Solar Probe Mission and the SWEAP team led by J. Kasper for use of data.

Solar Orbiter is a mission of international cooperation between ESA and NASA, operated by ESA. Funding for SwRI was provided by NASA contract NNG10EK25C. Funding for the University of Michigan was provided through SwRI subcontract A99201MO. R.M.D. acknowledges support from NASA grant 80NSSC22K0204.

This work utilizes data produced collaboratively between Air Force Research Laboratory (AFRL) & the National Solar Observatory (NSO). The ADAPT model development is supported by AFRL. The input data utilized by ADAPT is obtained by NSO/NISP (NSO Integrated Synoptic Program). NSO is operated by the Association of Universities for Research in Astronomy (AURA), Inc., under a cooperative agreement with the National Science Foundation (NSF).

This work utilizes GONG data obtained by the NSO Integrated Synoptic Program, managed by the National Solar Observatory, which is operated by the Association of Universities for Research in Astronomy (AURA), Inc. under a cooperative agreement with the National Science Foundation and with contribution from the National Oceanic and Atmospheric Administration. The GONG network of instruments is hosted by the Big Bear Solar Observatory, High Altitude Observatory, Learmonth Solar Observatory, Udaipur Solar Observatory, Instituto de Astrofísica de Canarias, and Cerro Tololo Interamerican Observatory.

SDO/AIA and SDO/HMI data is courtesy of NASA/SDO and the AIA, EVE, and HMI science teams.

This research used version 4.1.6 of the SunPy open source software package (Community et al. 2020), and made use of Heliopy, a community-developed Python package for space physics (Stansby et al. 2022). All code to replicate figures can be found at https://www.github.com/tamarervin/publications/e11_conjunction.

Software: Astropy (Astropy Collaboration et al. 2013, 2018, 2022), heliopy (Stansby et al. 2022), matplotlib (Hunter 2007), numpy (Harris et al. 2020), pandas (Wes McKinney 2010), psipy (Riley 2021), pfsspy (Stansby et al. 2020), scipy (Virtanen et al. 2020), spiceypy (Annex et al. 2020), SunPy (Community et al. 2020)

8. APPENDIX A: ALFVÉNICITY

We validate our cross helicity and residual energy results by looking at Figure 8. The cross helicity gives information about the level of Alfvénic fluctuations in the plasma while the residual energy is the difference between the magnetic and kinetic energy. We expect a circular shape when the cross helicity (σ_C) is plotted against the residual energy (σ_R), which we see in Figure 8 and is a validation of the cross helicity calculation we used to determine Alfvénicity of the plasma.

Figure 8 also shows the degradation of the measure of cross helicity as a tool to quantify Alfvénicity between PSP and Solar Orbiter. In the PSP measurements, we see the HCS plasma with a σ_C near 0 and σ_R values near -1. We expect HCS plasma to have low Alfvénicity ($\sigma_C \sim 0$) as it is a source of SSW and $\sigma_R \sim -1$ implies it is strongly dominated by magnetic field fluctuations. The SASW (purple) shows high levels of Alfvénicity in the PSP data ($\sigma_C \sim -1$) while in the Solar Orbiter data, it has a cross helicity value closer to 0. The FSW shows less differentiation between the PSP and Solar Orbiter measurements, in both cases with high σ_C and σ_R values near 0. The high Alfvénicity populations show σ_R values near 0, meaning there is a rough balance between magnetic and kinetic energy, implying nearly pure Alfvén fluctuations close to the Sun (Kasper et al. 2019). Overall, we see that the cross helicity measure becomes erased further from the Sun, proving the necessity of using both PSP and Solar Orbiter measurements to study this time period. This also shows some of the radial propagation effects of cross helicity and should be studied more fully with future multi-spacecraft conjunctions.

9. APPENDIX B: MAGNETIC FIELD MODELING

Our work relies upon two primary methods for modeling the solar coronal magnetic field. Both PFSS and MHD models have been shown to reproduce observed magnetic fields (Badman et al. 2020) and are a trusted method for determining the source origin of observed plasma. In Figure 9, we show a comparison of the radial cuts of the MHD model at $13.3R_\odot$ (closest radial cut of the model to the PSP perihelion distance), as discussed in section 3.2, with in-situ measurements.

The top panel shows a radial cut at $13.03R_\odot$ of the radial velocity as modeled by MAS, along with the modeled HCS (in black). We see regions of faster wind emerging from between streamer arcs. In the middle panel, we show the radial cut of the density at $13.45R_\odot$ with density enhancements in the model corresponding to the HCS and streamer regions. In the bottom panel, we compare the model radial magnetic field at $13.45R_\odot$ with the measurements from

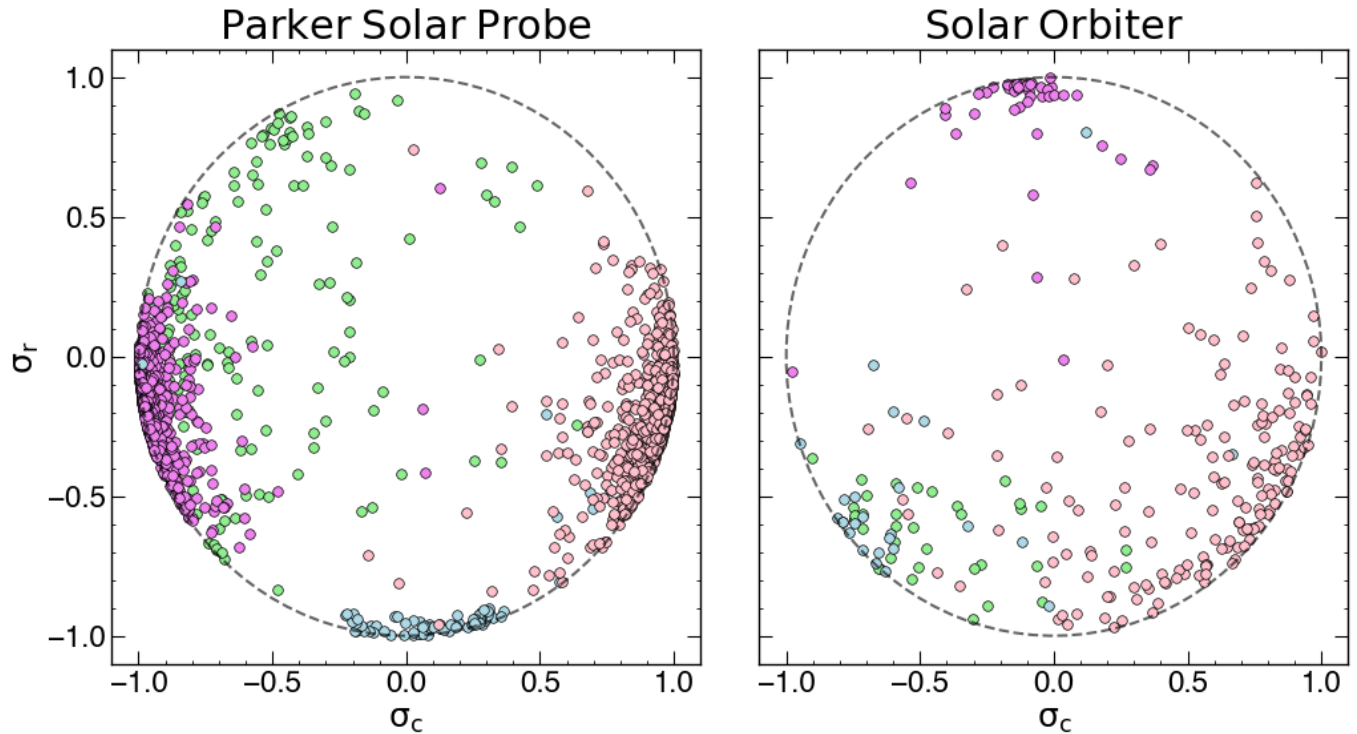


Figure 8. Comparison of the cross helicity (σ_C) and residual energy (σ_R). Points are colored based on the region of interest they correspond to. SSW is in green, SASW is in purple, FSW is in pink, and HCS wind is in blue. The dotted circle signifies the region within which we expect points to lie as $\sigma_C^2 + \sigma_R^2 \leq 1$ (Bavassano et al. 1998).

PSP/FIELDS. We see in situ enhancements corresponding to the model enhancements and the PSP trajectory crossing pseudostreamer arcs around 165° , giving us another look at the model and a way to understand the coronal field at this time.

In Figure 10, we compare estimated footpoints from the PFSS modeling method with footpoints produced with some random noise. We compare footpoints produced with noise both in the PSP velocity measurement used for the ballistic propagation model, along with errors in footpoints from adding $\pm 5^\circ$ in variation of the longitude and latitude source surface points. Similar to Figure 3, we see the jump in footpoints at $\sim 165^\circ$ characteristic of a streamer crossing, and that these errors do not impact the resulting source region of the observed solar wind at PSP and Solar Orbiter.

REFERENCES

- Abbo, L., Lionello, R., Riley, P., & Wang, Y. M. 2015, *SoPh*, 290, 2043, doi: [10.1007/s11207-015-0723-y](https://doi.org/10.1007/s11207-015-0723-y)
- Abbo, L., Ofman, L., Antiochos, S. K., et al. 2016, *SSRv*, 201, 55, doi: [10.1007/s11214-016-0264-1](https://doi.org/10.1007/s11214-016-0264-1)
- Alterman, B. L., & Kasper, J. C. 2019, *The Astrophysical Journal Letters*, 879, L6, doi: [10.3847/2041-8213/ab2391](https://doi.org/10.3847/2041-8213/ab2391)
- Alterman, B. L., Kasper, J. C., Stevens, M. L., & Koval, A. 2018, *ApJ*, 864, 112, doi: [10.3847/1538-4357/aad23f](https://doi.org/10.3847/1538-4357/aad23f)
- Altschuler, M. D., & Newkirk, G. 1969, *SoPh*, 9, 131, doi: [10.1007/BF00145734](https://doi.org/10.1007/BF00145734)
- Annex, A., Pearson, B., Seignovert, B., et al. 2020, *The Journal of Open Source Software*, 5, 2050, doi: [10.21105/joss.02050](https://doi.org/10.21105/joss.02050)
- Antiochos, S. K., Linker, J. A., Lionello, R., et al. 2012, *SSRv*, 172, 169, doi: [10.1007/s11214-011-9795-7](https://doi.org/10.1007/s11214-011-9795-7)
- Antiochos, S. K., Mikić, Z., Titov, V. S., Lionello, R., & Linker, J. A. 2011, *ApJ*, 731, 112, doi: [10.1088/0004-637X/731/2/112](https://doi.org/10.1088/0004-637X/731/2/112)
- Arge, C. N., Henney, C. J., Hernandez, I. G., et al. 2013, in *American Institute of Physics Conference Series*, Vol. 1539, *Solar Wind 13*, ed. G. P. Zank, J. Borovsky, R. Bruno, J. Cirtain, S. Cranmer, H. Elliott, J. Giacalone, W. Gonzalez, G. Li, E. Marsch, E. Moebius, N. Pogorelov, J. Spann, & O. Verkhoglyadova, 11–14, doi: [10.1063/1.4810977](https://doi.org/10.1063/1.4810977)

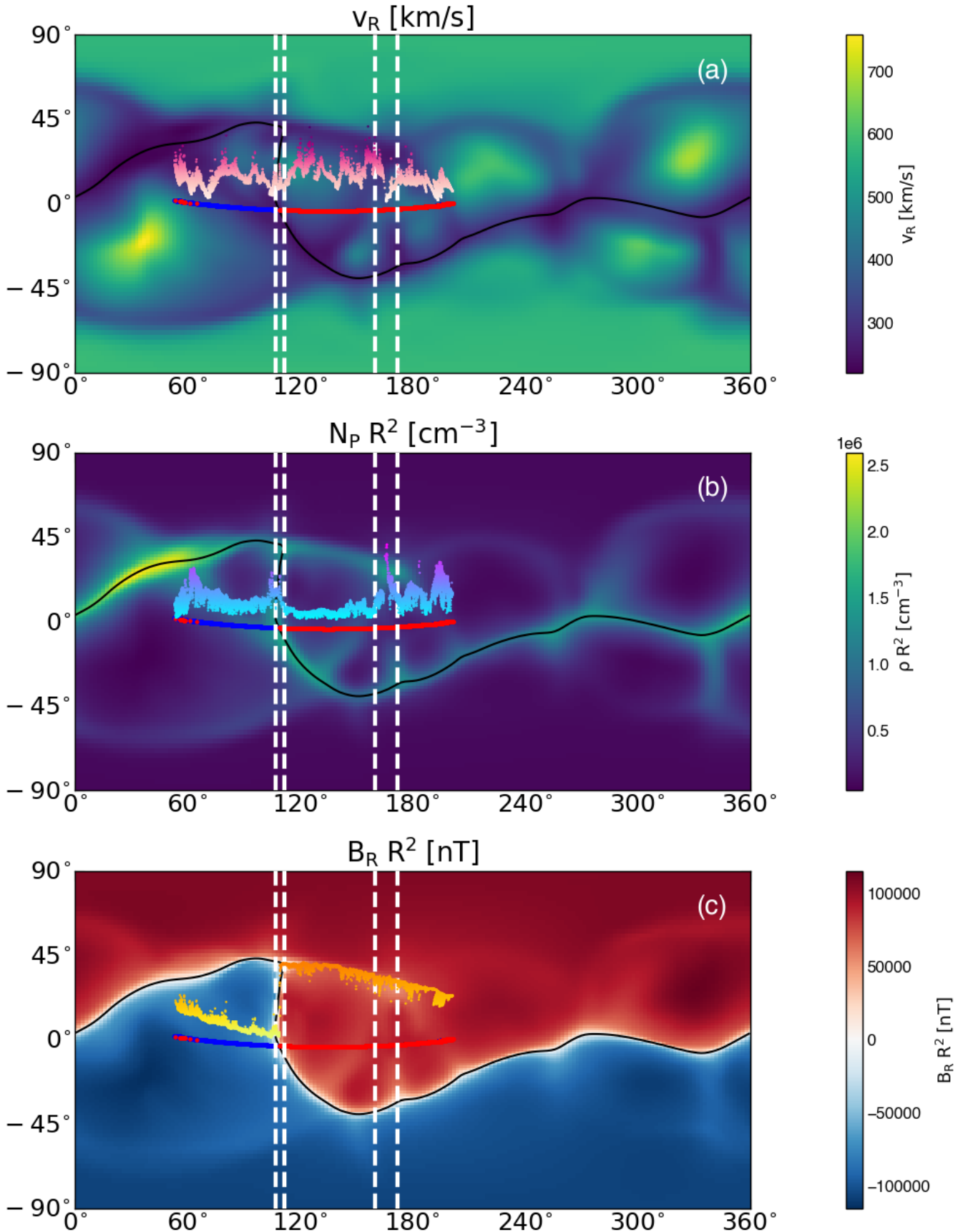


Figure 9. Radial cuts of the MAS MHD model (Riley et al. 2021) for PSP E11 using a SDO/HMI magnetogram from February 24, 2022 as the input boundary condition. The top panel shows the modeled radial velocity, middle panel shows the modeled density and the bottom panel shows the modeled radial magnetic field. We overlay the trajectory of PSP during E11 color-coded by the measured magnetic field polarity. The neutral line from the model is shown in black. We include in situ measurements of solar wind velocity, scaled proton density, and the radial magnetic field from PSP/FIELDS. The dotted white lines around 115° outline the HCS region, and the dotted white lines around 165° outline the pseudostreamer region.

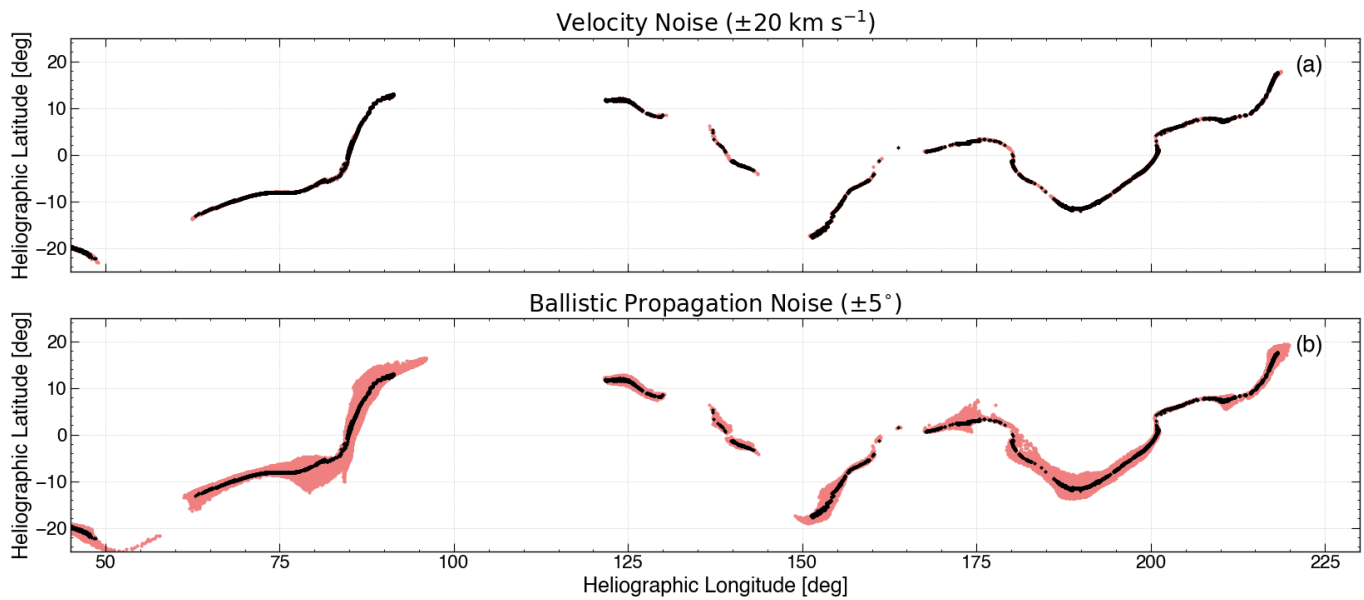


Figure 10. Comparison of the estimated PFSS footpoints used for this study (black) with footpoints estimated with different induced errors (shown in pink). *Panel (a):* PFSS footpoint estimations with $\pm 20 \text{ km s}^{-1}$ of random noise induced in the PSP radial velocity measurement used for ballistic propagation. *Panel (b):* PFSS footpoint estimations with $\pm 5^\circ$ of random noise induced in the source surface location based on ballistic propagation.

- Arge, C. N., Henney, C. J., Koller, J., et al. 2010, in American Institute of Physics Conference Series, Vol. 1216, Twelfth International Solar Wind Conference, ed. M. Maksimovic, K. Issautier, N. Meyer-Vernet, M. Moncuquet, & F. Pantellini, 343–346, doi: [10.1063/1.3395870](https://doi.org/10.1063/1.3395870)
- Arge, C. N., Henney, C. J., Koller, J., et al. 2011, in Astronomical Society of the Pacific Conference Series, Vol. 444, 5th International Conference of Numerical Modeling of Space Plasma Flows (ASTRONUM 2010), ed. N. V. Pogorelov, E. Audit, & G. P. Zank, 99
- Arge, C. N., Luhmann, J. G., Odstrcil, D., Schrijver, C. J., & Li, Y. 2004, *Journal of Atmospheric and Solar-Terrestrial Physics*, 66, 1295, doi: [10.1016/j.jastp.2004.03.018](https://doi.org/10.1016/j.jastp.2004.03.018)
- Arge, C. N., Odstrcil, D., Pizzo, V. J., & Mayer, L. R. 2003, *AIP Conference Proceedings*, 679, 190, doi: [10.1063/1.1618574](https://doi.org/10.1063/1.1618574)
- Arge, C. N., & Pizzo, V. J. 2000, *J. Geophys. Res.*, 105, 10465, doi: [10.1029/1999JA000262](https://doi.org/10.1029/1999JA000262)
- Asplund, M., Amarsi, A. M., & Grevesse, N. 2021, *A&A*, 653, A141, doi: [10.1051/0004-6361/202140445](https://doi.org/10.1051/0004-6361/202140445)
- Asplund, M., Grevesse, N., Sauval, A. J., & Scott, P. 2009, *ARA&A*, 47, 481, doi: [10.1146/annurev.astro.46.060407.145222](https://doi.org/10.1146/annurev.astro.46.060407.145222)
- Astropy Collaboration, Robitaille, T. P., Tollerud, E. J., et al. 2013, *A&A*, 558, A33, doi: [10.1051/0004-6361/201322068](https://doi.org/10.1051/0004-6361/201322068)
- Astropy Collaboration, Price-Whelan, A. M., Sipőcz, B. M., et al. 2018, *AJ*, 156, 123, doi: [10.3847/1538-3881/aabc4f](https://doi.org/10.3847/1538-3881/aabc4f)
- Astropy Collaboration, Price-Whelan, A. M., Lim, P. L., et al. 2022, *ApJ*, 935, 167, doi: [10.3847/1538-4357/ac7c74](https://doi.org/10.3847/1538-4357/ac7c74)
- Badman, S. T., Bale, S. D., Martínez Oliveros, J. C., et al. 2020, *ApJS*, 246, 23, doi: [10.3847/1538-4365/ab4da7](https://doi.org/10.3847/1538-4365/ab4da7)
- Badman, S. T., Brooks, D. H., Poirier, N., et al. 2022, *ApJ*, 932, 135, doi: [10.3847/1538-4357/ac6610](https://doi.org/10.3847/1538-4357/ac6610)
- Badman, S. T., Riley, P., Jones, S. I., et al. 2023, *Journal of Geophysical Research (Space Physics)*, 128, e2023JA031359, doi: [10.1029/2023JA031359](https://doi.org/10.1029/2023JA031359)
- Bale, S. D., Goetz, K., Harvey, P. R., et al. 2016, *SSRv*, 204, 49, doi: [10.1007/s11214-016-0244-5](https://doi.org/10.1007/s11214-016-0244-5)
- Bame, S. J., Asbridge, J. R., Feldman, W. C., & Gosling, J. T. 1977, *J. Geophys. Res.*, 82, 1487, doi: [10.1029/JA082i010p01487](https://doi.org/10.1029/JA082i010p01487)
- Bavassano, B., Pietropaolo, E., & Bruno, R. 1998, *J. Geophys. Res.*, 103, 6521, doi: [10.1029/97JA03029](https://doi.org/10.1029/97JA03029)
- Bavassano, B., Woo, R., & Bruno, R. 1997, *Geophys. Res. Lett.*, 24, 1655, doi: [10.1029/97GL01630](https://doi.org/10.1029/97GL01630)
- Bochsler, P. 2007, *A&A*, 471, 315, doi: [10.1051/0004-6361:20077772](https://doi.org/10.1051/0004-6361:20077772)
- Bochsler, P., Geiss, J., & Kunz, S. 1986, *SoPh*, 103, 177, doi: [10.1007/BF00154867](https://doi.org/10.1007/BF00154867)
- Borovsky, J. E. 2012, *Journal of Geophysical Research: Space Physics*, 117, doi: <https://doi.org/10.1029/2012JA017525>

- Borrini, G., Gosling, J. T., Bame, S. J., Feldman, W. C., & Wilcox, J. M. 1981, *J. Geophys. Res.*, 86, 4565, doi: [10.1029/JA086iA06p04565](https://doi.org/10.1029/JA086iA06p04565)
- Bruno, R., Villante, U., Bavassano, B., Schwenn, R., & Mariani, F. 1986, *SoPh*, 104, 431, doi: [10.1007/BF00159093](https://doi.org/10.1007/BF00159093)
- Buergi, A., & Geiss, J. 1986, *SoPh*, 103, 347, doi: [10.1007/BF00147835](https://doi.org/10.1007/BF00147835)
- Chen, C. H. K., Bale, S. D., Salem, C. S., & Maruca, B. A. 2013, *The Astrophysical Journal*, 770, 125, doi: [10.1088/0004-637X/770/2/125](https://doi.org/10.1088/0004-637X/770/2/125)
- Chen, C. H. K., Chandran, B. D. G., Woodham, L. D., et al. 2021, *A&A*, 650, L3, doi: [10.1051/0004-6361/202039872](https://doi.org/10.1051/0004-6361/202039872)
- Chen, Y., Esser, R., & Hu, Y. 2003, *ApJ*, 582, 467, doi: [10.1086/344642](https://doi.org/10.1086/344642)
- Chitta, L. P., Seaton, D. B., Downs, C., DeForest, C. E., & Higginson, A. K. 2023, *Nature Astronomy*, 7, 133, doi: [10.1038/s41550-022-01834-5](https://doi.org/10.1038/s41550-022-01834-5)
- Community, T. S., Barnes, W. T., Bobra, M. G., et al. 2020, *The Astrophysical Journal*, 890, 68, doi: [10.3847/1538-4357/ab4f7a](https://doi.org/10.3847/1538-4357/ab4f7a)
- Cranmer, S. R., & Winebarger, A. R. 2019, *Annual Review of Astronomy and Astrophysics*, 57, 157, doi: [10.1146/annurev-astro-091918-104416](https://doi.org/10.1146/annurev-astro-091918-104416)
- Crooker, N. U., Antiochos, S. K., Zhao, X., & Neugebauer, M. 2012, *Journal of Geophysical Research (Space Physics)*, 117, A04104, doi: [10.1029/2011JA017236](https://doi.org/10.1029/2011JA017236)
- Culhane, J. L., Brooks, D. H., van Driel-Gesztelyi, L., et al. 2014, *SoPh*, 289, 3799, doi: [10.1007/s11207-014-0551-5](https://doi.org/10.1007/s11207-014-0551-5)
- D'Amicis, R., & Bruno, R. 2015, *ApJ*, 805, 84, doi: [10.1088/0004-637X/805/1/84](https://doi.org/10.1088/0004-637X/805/1/84)
- D'Amicis, R., Matteini, L., & Bruno, R. 2018, *Monthly Notices of the Royal Astronomical Society*, 483, 4665, doi: [10.1093/mnras/sty3329](https://doi.org/10.1093/mnras/sty3329)
- D'Amicis, R., Perrone, D., Bruno, R., & Velli, M. 2021, *Journal of Geophysical Research: Space Physics*, 126, e2020JA028996, doi: [https://doi.org/10.1029/2020JA028996](https://doi.org/https://doi.org/10.1029/2020JA028996)
- D'Amicis, R., Bruno, R., Panasenco, O., et al. 2021, *A&A*, 656, A21, doi: [10.1051/0004-6361/202140938](https://doi.org/10.1051/0004-6361/202140938)
- Elsasser, W. M. 1950, *Physical Review*, 79, 183, doi: [10.1103/PhysRev.79.183](https://doi.org/10.1103/PhysRev.79.183)
- Eselevich, V. G., Fainshtein, V. G., & Rudenko, G. V. 1999, *SoPh*, 188, 277, doi: [10.1023/A:1005216707272](https://doi.org/10.1023/A:1005216707272)
- Feldman, U. 1992, *PhyS*, 46, 202, doi: [10.1088/0031-8949/46/3/002](https://doi.org/10.1088/0031-8949/46/3/002)
- Feldman, U., & Laming, J. M. 2000, *PhyS*, 61, 222, doi: [10.1238/Physica.Regular.061a00222](https://doi.org/10.1238/Physica.Regular.061a00222)
- Feldman, W. C., & Marsch, E. 1997, in *Cosmic Winds and the Heliosphere*, 617
- Fox, N. J., Velli, M. C., Bale, S. D., et al. 2016, *SSRv*, 204, 7, doi: [10.1007/s11214-015-0211-6](https://doi.org/10.1007/s11214-015-0211-6)
- Garton, T. M., Murray, S. A., & Gallagher, P. T. 2018, *The Astrophysical Journal Letters*, 869, L12, doi: [10.3847/2041-8213/aaf39a](https://doi.org/10.3847/2041-8213/aaf39a)
- Gary, S. P., Yin, L., Winske, D., & Reisenfeld, D. B. 2000, *Geophys. Res. Lett.*, 27, 1355, doi: [10.1029/2000GL000019](https://doi.org/10.1029/2000GL000019)
- Geiss, J., Gloeckler, G., & Von Steiger, R. 1995, *Space Science Reviews*, 72, 49, doi: [10.1007/BF00768753](https://doi.org/10.1007/BF00768753)
- Gloeckler, G., & Geiss, J. 1989, in *American Institute of Physics Conference Series*, Vol. 183, *Cosmic Abundances of Matter*, ed. C. J. Waddington, 49–71, doi: [10.1063/1.37985](https://doi.org/10.1063/1.37985)
- Gosling, J. T., Borrini, G., Asbridge, J. R., et al. 1981, *J. Geophys. Res.*, 86, 5438, doi: [10.1029/JA086iA07p05438](https://doi.org/10.1029/JA086iA07p05438)
- Harris, C. R., Millman, K. J., van der Walt, S. J., et al. 2020, *Nature*, 585, 357, doi: [10.1038/s41586-020-2649-2](https://doi.org/10.1038/s41586-020-2649-2)
- Harvey, J. W., Hill, F., Hubbard, R. P., et al. 1996, *Science*, 272, 1284, doi: [10.1126/science.272.5266.1284](https://doi.org/10.1126/science.272.5266.1284)
- Hickmann, K. S., Godinez, H. C., Henney, C. J., & Arge, C. N. 2015, *Solar Physics*, 290, 1105, doi: [10.1007/s11207-015-0666-3](https://doi.org/10.1007/s11207-015-0666-3)
- Hoeksema, J. T. 1984, PhD thesis, Stanford University, California
- Horbury, T. S., O'Brien, H., Carrasco Blazquez, I., et al. 2020, *A&A*, 642, A9, doi: [10.1051/0004-6361/201937257](https://doi.org/10.1051/0004-6361/201937257)
- Howard, R. A., Moses, J. D., Vourlidas, A., et al. 2008, *SSRv*, 136, 67, doi: [10.1007/s11214-008-9341-4](https://doi.org/10.1007/s11214-008-9341-4)
- Hundhausen, A. J. 1968, *Space Science Reviews*, 8, 690, doi: [10.1007/BF00175116](https://doi.org/10.1007/BF00175116)
- Hunter, J. D. 2007, *Computing in Science & Engineering*, 9, 90, doi: [10.1109/MCSE.2007.55](https://doi.org/10.1109/MCSE.2007.55)
- Kasper, J. C., Stevens, M. L., Korreck, K. E., et al. 2012, *The Astrophysical Journal*, 745, 162, doi: [10.1088/0004-637X/745/2/162](https://doi.org/10.1088/0004-637X/745/2/162)
- Kasper, J. C., Stevens, M. L., Lazarus, A. J., Steinberg, J. T., & Ogilvie, K. W. 2007, *ApJ*, 660, 901, doi: [10.1086/510842](https://doi.org/10.1086/510842)
- Kasper, J. C., Abiad, R., Austin, G., et al. 2016, *Space Science Reviews*, 204, 131, doi: [10.1007/s11214-015-0206-3](https://doi.org/10.1007/s11214-015-0206-3)
- Kasper, J. C., Bale, S. D., Belcher, J. W., et al. 2019, *Nature*, 576, 228, doi: [10.1038/s41586-019-1813-z](https://doi.org/10.1038/s41586-019-1813-z)
- Ko, Y.-K., Muglach, K., Wang, Y.-M., Young, P. R., & Lepri, S. T. 2014, *ApJ*, 787, 121, doi: [10.1088/0004-637X/787/2/121](https://doi.org/10.1088/0004-637X/787/2/121)

- Ko, Y.-K., Raymond, J. C., Zurbuchen, T. H., et al. 2006, *ApJ*, 646, 1275, doi: [10.1086/505021](https://doi.org/10.1086/505021)
- Koukras, A., Dolla, L., & Keppens, R. 2022, in SHINE 2022 Workshop, 68, doi: [10.48550/arXiv.2212.11553](https://doi.org/10.48550/arXiv.2212.11553)
- Laming, J. M. 2015, *Living Reviews in Solar Physics*, 12, 2, doi: [10.1007/lrsp-2015-2](https://doi.org/10.1007/lrsp-2015-2)
- Laming, J. M. 2017, *ApJ*, 844, 153, doi: [10.3847/1538-4357/aa7cfl](https://doi.org/10.3847/1538-4357/aa7cfl)
- Laming, J. M., Vourlidas, A., Korendyke, C., et al. 2019, *ApJ*, 879, 124, doi: [10.3847/1538-4357/ab23fl](https://doi.org/10.3847/1538-4357/ab23fl)
- Landi, E., Gruesbeck, J. R., Lepri, S. T., Zurbuchen, T. H., & Fisk, L. A. 2012, *ApJ*, 761, 48, doi: [10.1088/0004-637X/761/1/48](https://doi.org/10.1088/0004-637X/761/1/48)
- Leer, E., & Holzer, T. E. 1980, *J. Geophys. Res.*, 85, 4681, doi: [10.1029/JA085iA09p04681](https://doi.org/10.1029/JA085iA09p04681)
- Lemen, J. R., Title, A. M., Akin, D. J., et al. 2012, *SoPh*, 275, 17, doi: [10.1007/s11207-011-9776-8](https://doi.org/10.1007/s11207-011-9776-8)
- Liewer, P. C., Neugebauer, M., & Zurbuchen, T. 2003, in *American Institute of Physics Conference Series*, Vol. 679, *Solar Wind Ten*, ed. M. Velli, R. Bruno, F. Malara, & B. Bucci, 51–54, doi: [10.1063/1.1618539](https://doi.org/10.1063/1.1618539)
- Liewer, P. C., Vourlidas, A., Stenborg, G., et al. 2023, *The Astrophysical Journal*, 948, 24, doi: [10.3847/1538-4357/acc8c7](https://doi.org/10.3847/1538-4357/acc8c7)
- Lionello, R., Linker, J. A., & Mikić, Z. 2001, *The Astrophysical Journal*, 546, 542, doi: [10.1086/318254](https://doi.org/10.1086/318254)
- . 2008, *The Astrophysical Journal*, 690, 902, doi: [10.1088/0004-637X/690/1/902](https://doi.org/10.1088/0004-637X/690/1/902)
- Lionello, R., Riley, P., Linker, J. A., & Mikić, Z. 2005, *ApJ*, 625, 463, doi: [10.1086/429268](https://doi.org/10.1086/429268)
- Livi, R., Larson, D. E., Kasper, J. C., et al. 2022, *The Astrophysical Journal*, 938, 138, doi: [10.3847/1538-4357/ac93f5](https://doi.org/10.3847/1538-4357/ac93f5)
- Livi, S., Lepri, S. T., Raines, J. M., et al. 2023, *A&A*, 676, A36, doi: [10.1051/0004-6361/202346304](https://doi.org/10.1051/0004-6361/202346304)
- Lopez, R. E., & Freeman, J. W. 1986, *J. Geophys. Res.*, 91, 1701, doi: [10.1029/JA091iA02p01701](https://doi.org/10.1029/JA091iA02p01701)
- Lynch, B. J., Viall, N. M., Higginson, A. K., et al. 2023, *ApJ*, 949, 14, doi: [10.3847/1538-4357/acc38c](https://doi.org/10.3847/1538-4357/acc38c)
- Macneil, A. R., Owens, M. J., Finley, A. J., & Matt, S. P. 2022, *MNRAS*, 509, 2390, doi: [10.1093/mnras/stab2965](https://doi.org/10.1093/mnras/stab2965)
- Maksimovic, M., Bale, S. D., Chust, T., et al. 2021, *A&A*, 654, C2, doi: [10.1051/0004-6361/201936214e](https://doi.org/10.1051/0004-6361/201936214e)
- McComas, D. J., Ebert, R. W., Elliott, H. A., et al. 2008, *Geophys. Res. Lett.*, 35, L18103, doi: [10.1029/2008GL034896](https://doi.org/10.1029/2008GL034896)
- McComas, D. J., Goldstein, R., Gosling, J. T., & Skoug, R. M. 2001, *SSRv*, 97, 99, doi: [10.1023/A:1011826111330](https://doi.org/10.1023/A:1011826111330)
- McComas, D. J., Riley, P., Gosling, J. T., Balogh, A., & Forsyth, R. 1998, *J. Geophys. Res.*, 103, 1955, doi: [10.1029/97JA01459](https://doi.org/10.1029/97JA01459)
- McComas, D. J., Alexander, N., Angold, N., et al. 2016, *Space Science Reviews*, 204, 187, doi: [10.1007/s11214-014-0059-1](https://doi.org/10.1007/s11214-014-0059-1)
- Meyer, J. P. 1985, *ApJS*, 57, 151, doi: [10.1086/191000](https://doi.org/10.1086/191000)
- Mostafavi, P., Allen, R. C., McManus, M. D., et al. 2022, *The Astrophysical Journal Letters*, 926, L38, doi: [10.3847/2041-8213/ac51e1](https://doi.org/10.3847/2041-8213/ac51e1)
- Müller, D., St. Cyr, O. C., Zouganelis, I., et al. 2020, *A&A*, 642, A1, doi: [10.1051/0004-6361/202038467](https://doi.org/10.1051/0004-6361/202038467)
- Nolte, J. T., & Roelof, E. C. 1973, *SoPh*, 33, 241, doi: [10.1007/BF00152395](https://doi.org/10.1007/BF00152395)
- Nolte, J. T., Krieger, A. S., Timothy, A. F., et al. 1976, *SoPh*, 46, 303, doi: [10.1007/BF00149859](https://doi.org/10.1007/BF00149859)
- Ohmi, T., Kojima, M., Tokumaru, M., Fujiki, K., & Hakamada, K. 2004, *Advances in Space Research*, 33, 689, doi: [https://doi.org/10.1016/S0273-1177\(03\)00238-2](https://doi.org/10.1016/S0273-1177(03)00238-2)
- Owen, C. J., Bruno, R., Livi, S., et al. 2020, *A&A*, 642, A16, doi: [10.1051/0004-6361/201937259](https://doi.org/10.1051/0004-6361/201937259)
- Owens, M. J. 2018, *Solar Physics*, 293, 122, doi: [10.1007/s11207-018-1343-0](https://doi.org/10.1007/s11207-018-1343-0)
- Owens, M. J., Crooker, N. U., & Lockwood, M. 2014, *Journal of Geophysical Research (Space Physics)*, 119, 36, doi: [10.1002/2013JA019412](https://doi.org/10.1002/2013JA019412)
- Owocik, S. P., Holzer, T. E., & Hundhausen, A. J. 1983, *ApJ*, 275, 354, doi: [10.1086/161538](https://doi.org/10.1086/161538)
- Panasenco, O., Martin, S. F., Velli, M., & Vourlidas, A. 2013, *SoPh*, 287, 391, doi: [10.1007/s11207-012-0194-3](https://doi.org/10.1007/s11207-012-0194-3)
- Panasenco, O., & Velli, M. 2013, in *American Institute of Physics Conference Series*, Vol. 1539, *Solar Wind 13*, ed. G. P. Zank, J. Borovsky, R. Bruno, J. Cirtain, S. Cranmer, H. Elliott, J. Giacalone, W. Gonzalez, G. Li, E. Marsch, E. Moebius, N. Pogorelov, J. Spann, & O. Verkhoglyadova, 50–53, doi: [10.1063/1.4810987](https://doi.org/10.1063/1.4810987)
- Panasenco, O., Velli, M., & Panasenco, A. 2019, *ApJ*, 873, 25, doi: [10.3847/1538-4357/ab017c](https://doi.org/10.3847/1538-4357/ab017c)
- Panasenco, O., Velli, M., D’Amicis, R., et al. 2020, *ApJS*, 246, 54, doi: [10.3847/1538-4365/ab61f4](https://doi.org/10.3847/1538-4365/ab61f4)
- Parker, E. N. 1958, *ApJ*, 128, 664, doi: [10.1086/146579](https://doi.org/10.1086/146579)
- Perrone, D., D’Amicis, R., De Marco, R., et al. 2020, *A&A*, 633, A166, doi: [10.1051/0004-6361/201937064](https://doi.org/10.1051/0004-6361/201937064)
- Pesnell, W. D., Thompson, B. J., & Chamberlin, P. C. 2012, *SoPh*, 275, 3, doi: [10.1007/s11207-011-9841-3](https://doi.org/10.1007/s11207-011-9841-3)
- Pulupa, M., Bale, S. D., Bonnell, J. W., et al. 2017, *Journal of Geophysical Research (Space Physics)*, 122, 2836, doi: [10.1002/2016JA023345](https://doi.org/10.1002/2016JA023345)
- Riley, P. 2021, *EDP Sciences for European Southern Observatory*.

- Riley, P., Linker, J. A., & Arge, C. N. 2015, *Space Weather*, 13, 154, doi: [10.1002/2014SW001144](https://doi.org/10.1002/2014SW001144)
- Riley, P., Linker, J. A., Mikić, Z., et al. 2006, *ApJ*, 653, 1510, doi: [10.1086/508565](https://doi.org/10.1086/508565)
- Riley, P., Lionello, R., Caplan, R. M., et al. 2021, *A&A*, 650, A19, doi: [10.1051/0004-6361/202039815](https://doi.org/10.1051/0004-6361/202039815)
- Riley, P., & Luhmann, J. G. 2012, *SoPh*, 277, 355, doi: [10.1007/s11207-011-9909-0](https://doi.org/10.1007/s11207-011-9909-0)
- Rivera, Y. J., Badman, S. T., & Stevens, M. L. Submitted, *Science*
- Rivera, Y. J., Lepri, S. T., Raymond, J. C., et al. 2021, *ApJ*, 921, 93, doi: [10.3847/1538-4357/ac1676](https://doi.org/10.3847/1538-4357/ac1676)
- Rodríguez-Pacheco, J., Wimmer-Schweingruber, R. F., Mason, G. M., et al. 2020, *A&A*, 642, A7, doi: [10.1051/0004-6361/201935287](https://doi.org/10.1051/0004-6361/201935287)
- Romeo, O. M., Braga, C. R., Badman, S. T., et al. 2023, *The Astrophysical Journal*, 954, 168, doi: [10.3847/1538-4357/ace62e](https://doi.org/10.3847/1538-4357/ace62e)
- Rouillard, A. P., Davies, J. A., Lavraud, B., et al. 2010, *Journal of Geophysical Research (Space Physics)*, 115, A04103, doi: [10.1029/2009JA014471](https://doi.org/10.1029/2009JA014471)
- Schatten, K. H., Wilcox, J. M., & Ness, N. F. 1969, *SoPh*, 6, 442, doi: [10.1007/BF00146478](https://doi.org/10.1007/BF00146478)
- Scherrer, P. H., Schou, J., Bush, R. I., et al. 2012, *SoPh*, 275, 207, doi: [10.1007/s11207-011-9834-2](https://doi.org/10.1007/s11207-011-9834-2)
- Schwenn, R. 2006, *SSRv*, 124, 51, doi: [10.1007/s11214-006-9099-5](https://doi.org/10.1007/s11214-006-9099-5)
- Sheeley, N. R., J., Lee, D. D. H., Casto, K. P., Wang, Y. M., & Rich, N. B. 2009, *ApJ*, 694, 1471, doi: [10.1088/0004-637X/694/2/1471](https://doi.org/10.1088/0004-637X/694/2/1471)
- Sheeley, N. R., J., Martin, S. F., Panasenco, O., & Warren, H. P. 2013, *ApJ*, 772, 88, doi: [10.1088/0004-637X/772/2/88](https://doi.org/10.1088/0004-637X/772/2/88)
- Sheeley, N. R., Wang, Y. M., Hawley, S. H., et al. 1997, *ApJ*, 484, 472, doi: [10.1086/304338](https://doi.org/10.1086/304338)
- Smith, E. J., Tsurutani, B. T., & Rosenberg, R. L. 1978, *J. Geophys. Res.*, 83, 717, doi: [10.1029/JA083iA02p00717](https://doi.org/10.1029/JA083iA02p00717)
- Snyder, C. W., & Neugebauer, M. 1966, *The Solar Wind* (Pergamon Press)
- Stakhiv, M., Landi, E., Lepri, S. T., Oran, R., & Zurbuchen, T. H. 2015, *ApJ*, 801, 100, doi: [10.1088/0004-637X/801/2/100](https://doi.org/10.1088/0004-637X/801/2/100)
- Stansby, D., Baker, D., Brooks, D. H., & Owen, C. J. 2020a, *A&A*, 640, A28, doi: [10.1051/0004-6361/202038319](https://doi.org/10.1051/0004-6361/202038319)
- Stansby, D., Green, L. M., van Driel-Gesztelyi, L., & Horbury, T. S. 2021, *Solar Physics*, 296, 116, doi: [10.1007/s11207-021-01861-x](https://doi.org/10.1007/s11207-021-01861-x)
- Stansby, D., Horbury, T. S., & Matteini, L. 2018, *Monthly Notices of the Royal Astronomical Society*, 482, 1706, doi: [10.1093/mnras/sty2814](https://doi.org/10.1093/mnras/sty2814)
- Stansby, D., Matteini, L., Horbury, T. S., et al. 2020b, *MNRAS*, 492, 39, doi: [10.1093/mnras/stz3422](https://doi.org/10.1093/mnras/stz3422)
- Stansby, D., Yeates, A., & Badman, S. 2020, *Journal of Open Source Software*, 5, 2732, doi: [10.21105/joss.02732](https://doi.org/10.21105/joss.02732)
- Stansby, D., Rai, Y., Argall, M., et al. 2022
- Suess, S. T., Ko, Y. K., von Steiger, R., & Moore, R. L. 2009, *Journal of Geophysical Research (Space Physics)*, 114, A04103, doi: [10.1029/2008JA013704](https://doi.org/10.1029/2008JA013704)
- Telloni, D., Romoli, M., Velli, M., et al. 2023, *ApJL*, 955, L4, doi: [10.3847/2041-8213/ace112](https://doi.org/10.3847/2041-8213/ace112)
- Tu, C. Y., & Marsch, E. 1995, *SSRv*, 73, 1, doi: [10.1007/BF00748891](https://doi.org/10.1007/BF00748891)
- Velli, M., Harra, L. K., Vourlidas, A., et al. 2020, *A&A*, 642, A4, doi: [10.1051/0004-6361/202038245](https://doi.org/10.1051/0004-6361/202038245)
- Viall, N. M., & Borovsky, J. E. 2020, *Journal of Geophysical Research (Space Physics)*, 125, e26005, doi: [10.1029/2018JA026005](https://doi.org/10.1029/2018JA026005)
- Virtanen, P., Gommers, R., Oliphant, T. E., et al. 2020, *Nature Methods*, 17, 261, doi: [10.1038/s41592-019-0686-2](https://doi.org/10.1038/s41592-019-0686-2)
- von Steiger, R., & Zurbuchen, T. H. 2011, *Journal of Geophysical Research (Space Physics)*, 116, A01105, doi: [10.1029/2010JA015835](https://doi.org/10.1029/2010JA015835)
- von Steiger, R., Schwadron, N. A., Fisk, L. A., et al. 2000, *Journal of Geophysical Research: Space Physics*, 105, 27217, doi: <https://doi.org/10.1029/1999JA000358>
- Vourlidas, A., Howard, R. A., Plunkett, S. P., et al. 2016, *Space Science Reviews*, 204, 83, doi: [10.1007/s11214-014-0114-y](https://doi.org/10.1007/s11214-014-0114-y)
- Wallace, S., Arge, C. N., Viall, N., & Pihlström, Y. 2020, *The Astrophysical Journal*, 898, 78, doi: [10.3847/1538-4357/ab98a0](https://doi.org/10.3847/1538-4357/ab98a0)
- Wang, Y. M. 2009, *SSRv*, 144, 383, doi: [10.1007/s11214-008-9434-0](https://doi.org/10.1007/s11214-008-9434-0)
- . 2013, *ApJL*, 775, L46, doi: [10.1088/2041-8205/775/2/L46](https://doi.org/10.1088/2041-8205/775/2/L46)
- . 2016, *ApJ*, 833, 121, doi: [10.3847/1538-4357/833/1/121](https://doi.org/10.3847/1538-4357/833/1/121)
- Wang, Y. M., Grappin, R., Robbrecht, E., & Sheeley, N. R., J. 2012, *ApJ*, 749, 182, doi: [10.1088/0004-637X/749/2/182](https://doi.org/10.1088/0004-637X/749/2/182)
- Wang, Y.-M., Ko, Y.-K., & Grappin, R. 2009, *The Astrophysical Journal*, 691, 760, doi: [10.1088/0004-637X/691/1/760](https://doi.org/10.1088/0004-637X/691/1/760)
- Wang, Y.-M., N. R. Sheeley, J., & Rich, N. B. 2007, *The Astrophysical Journal*, 658, 1340, doi: [10.1086/511416](https://doi.org/10.1086/511416)
- Wang, Y.-M., & Panasenco, O. 2019, *The Astrophysical Journal*, 872, 139, doi: [10.3847/1538-4357/aaff5e](https://doi.org/10.3847/1538-4357/aaff5e)
- Wang, Y. M., & Sheeley, N. R., J. 1990, *ApJ*, 355, 726, doi: [10.1086/168805](https://doi.org/10.1086/168805)
- . 1997, *Geophys. Res. Lett.*, 24, 3141, doi: [10.1029/97GL53305](https://doi.org/10.1029/97GL53305)

- Wang, Y. M., Sheeley, N. R., Socker, D. G., Howard, R. A., & Rich, N. B. 2000, *J. Geophys. Res.*, 105, 25133, doi: [10.1029/2000JA000149](https://doi.org/10.1029/2000JA000149)
- Wes McKinney. 2010, in *Proceedings of the 9th Python in Science Conference*, ed. Stéfan van der Walt & Jarrod Millman, 56 – 61, doi: [10.25080/Majora-92bf1922-00a](https://doi.org/10.25080/Majora-92bf1922-00a)
- Whittlesey, P. L., Larson, D. E., Kasper, J. C., et al. 2020, *The Astrophysical Journal Supplement Series*, 246, 74, doi: [10.3847/1538-4365/ab7370](https://doi.org/10.3847/1538-4365/ab7370)
- Wicks, R. T., Roberts, D. A., Mallet, A., et al. 2013, *The Astrophysical Journal*, 778, 177, doi: [10.1088/0004-637X/778/2/177](https://doi.org/10.1088/0004-637X/778/2/177)
- Widing, K. G., & Feldman, U. 2001, *ApJ*, 555, 426, doi: [10.1086/321482](https://doi.org/10.1086/321482)
- Worden, J., & Harvey, J. 2000, *Solar Physics*, 195, 247, doi: [10.1023/A:1005272502885](https://doi.org/10.1023/A:1005272502885)
- Zhao, L., & Fisk, L. 2011, *SoPh*, 274, 379, doi: [10.1007/s11207-011-9840-4](https://doi.org/10.1007/s11207-011-9840-4)
- Zhao, L., Landi, E., Lepri, S. T., et al. 2017, *The Astrophysical Journal Supplement Series*, 228, 4, doi: [10.3847/1538-4365/228/1/4](https://doi.org/10.3847/1538-4365/228/1/4)
- Zhao, L., Landi, E., Zurbuchen, T. H., Fisk, L. A., & Lepri, S. T. 2014, *ApJ*, 793, 44, doi: [10.1088/0004-637X/793/1/44](https://doi.org/10.1088/0004-637X/793/1/44)
- Zhao, L., Zurbuchen, T. H., & Fisk, L. A. 2009, *Geophys. Res. Lett.*, 36, L14104, doi: [10.1029/2009GL039181](https://doi.org/10.1029/2009GL039181)
- Zurbuchen, T. H. 2007, *ARA&A*, 45, 297, doi: [10.1146/annurev.astro.45.010807.154030](https://doi.org/10.1146/annurev.astro.45.010807.154030)